Clock Synchronization with Correlated Photons

Christopher Spiess,[1,2,*] Sebastian Töpfer,[2,3] Sakshi Sharma,[1,2] Andrej Kržič,[1,2] Meritxell Cabrejo-Ponce,[1,2] Uday Chandrashekara,[2] Nico Lennart Döll,[2] Daniel Rieländer,[2,4] and Fabian Steinlechner[2,5]

[1] *Friedrich Schiller University Jena, Fürstengraben 1, Jena 07743, Germany*
[2] *Fraunhofer Institute for Applied Optics and Precision Engineering, Albert-Einstein-Strasse 7, Jena 07745, Germany*
[3] *Institut für angewandte Physik, TU Darmstadt, Schlossgartenstrasse 7, 64289 Darmstadt*
[4] *European Space Operations Centre (ESOC), Robert-Bosch-Strasse 5, 64293 Darmstadt*
[5] *Friedrich Schiller University Jena, Abbe Center of Photonics, Albert-Einstein-Strasse 6, Jena 07745, Germany*

(Received 28 October 2022; revised 6 April 2023; accepted 14 April 2023; published 25 May 2023)

Event synchronization is a ubiquitous task, with applications ranging from 5G technology to industrial automation and smart power grids. The emergence of quantum communication networks will further increase the demand for precise synchronization in the optical and electronic domains, which implies significant resource overhead, such as the requirement for ultrastable clocks or additional synchronization lasers. Here, we show how temporal correlations of photons may be harnessed for synchronization in quantum networks. We achieve stable synchronization jitter <68 ps with as few as 44 correlated detection events per 100-ms data package and demonstrate feasibility in realistic emulated high-loss link scenarios, including atmospheric turbulence. In contrast to previous work, this is accomplished without any external timing reference and only simple crystal oscillators. Our approach replaces the optical and electronic transmission of timing signals with classical communication and computer-aided postprocessing. It can be easily integrated into a wide range of quantum communication networks and could pave the way to future applications in entanglement-based secure time transmission.

DOI: 10.1103/PhysRevApplied.19.054082

I. INTRODUCTION

Secure transmission of information and reliable event synchronization are key requirements in critical infrastructures [1,2], especially in power grids [3], financial networks [4], and cloud database services [5]. Regarding information security, quantum key distribution (QKD) offers the unique proposition of encryption keys the confidentiality of which can be lower bounded by the laws of physics [6–9]. Quantum communication is thus poised to become the backbone of a secure information infrastructure, with networks of many hundreds of fiber links established, and integration of ground-to-space relays over more than 1000 km already under way [10].

Quantum communication networks, which involve tight timing budgets in the optical and electronic domains, are also a prime example of the need for accurate synchronization of remote parties. In classical communication networks, the network time protocol (NTP) ensures synchronization with accuracy down to milliseconds [11] and the Global Navigation Satellite System (GNSS) [12] can reduce this to nanoseconds. Modern high-bit-rate QKD systems, however, operate at picosecond time scales and inevitably call for even better synchronization [13]. In state-of-the-art QKD experiments, this is typically achieved by auxiliary pulsed lasers [10,14,15] or stable references [16], such as rubidium clocks [17, 18] or GNSS [19–21]. Specialized classical infrastructure together with the White Rabbit protocol [22] may reach sufficient performance as well [23]. All together, the requirement for auxiliary components creates a resource overhead that reduces the scalability [24] of networks in fiber and even applicability in space, due to the tight constraints on power consumption and weight [25,26]. Moreover, much like the case of classical telecommunication networks, these requirements are likely to increase further when considering advanced network protocols, e.g., quantum teleportation [27,28] and entanglement swapping [29,30].

*christopher.spiess@iof.fraunhofer.de

Quantum clock synchronization protocols have been proposed to tackle the synchronization of distant clocks [31–33] in multipartite network settings [34,35] and with quantum enhancement beyond the possibilities of classical physics [36]. To this end, investigations over recent years have focused on the exploitation of the temporal correlations of photons [37–40], with ongoing research on the precision enhancement with nonclassical phenomena (such as the Hong-Ou-Mandel effect) or possibly entanglement. When photon pairs originate from a common creation event, this gives rise to a narrow correlation peak in their arrival time at remote receivers. In other words, the location of this correlation peak indicates the average time delay between the receivers and can thus be used to extract the time and frequency differences between remote clocks [41,42]. The recent past has seen further advancement, with experiments achieving exceptionally high precision with respect to a common frequency reference [43]: 600 fs with correlated photons [37] or down to 60 fs using Hong-Ou-Mandel interference [38–40]. In deployed long-distance links, synchronization jitters as low as a few tens of picoseconds have been demonstrated using ultraprecise rubidium clocks or Global-Positioning-System- (GPS) disciplined clocks [19,21,44]. Without atomic frequency references, the timing jitter is orders of magnitude higher (e.g., the frequency offset for standard crystal oscillators may be up to 8 orders of magnitude higher [45,46]). This frequency difference results in a temporal drift of the correlation peak and makes it impossible to find the initial timing offset for synchronization. This has limited the applicability of synchronization based purely on quantum correlations [42]. Additional rubidium clocks, GPS-disciplined clocks, or other common time references have long been a necessary requirement for deploying long-distance and high-bit-rate quantum communication systems [16,18,19,21].

In this paper, we build on the groundbreaking work of Ho *et al.* [42] and Valencia *et al.* [41] and establish the feasibility of picosecond-level synchronization using the correlations of photon pairs in realistic link scenarios. Unlike state-of-the-art field experiments, which employ active electro-optic modulation to actively encode synchronization sequences [47–49], we accomplish this purely in postprocessing, without any requirement for auxiliary hardware. Our protocol (Sec. II A) estimates the clock-frequency difference and compensates for the resulting broadening of correlation peaks (Sec. II B 1). This allows us to find the correlation peak, even in low signal-to-noise scenarios. Tracking the position of the correlation peak during the communication session allows us to correct for residual clock instabilities and achieve synchronization with root-mean-square (rms) jitters <68 ps (Sec. II B 2). What is remarkable is that the approach also works when the correlated detection events are as low as 440 ± 200 counts/s, as is expected in real lossy-link scenarios. Even more remarkably, these values are completely comparable to the (30–50)-ps jitters reported for systems that employ high-performance GPS-disciplined rubidium clocks [19,21]. Finally, we establish the feasibility of the protocol for communication links through a turbulent atmosphere, where channel fades have a major impact on the detected photons statistics (Sec. II C) [50].

The results of our proof-of-concept experiment show that time-correlated photon pairs can be a valuable resource for synchronization with minimal hardware overhead. The methods work not only for laboratory experiments but also for deployed QKD systems [51,52] in high-loss link scenarios. In this approach, synchronization is a by-product of the key exchange without compromising the secure key rate. It provides a simple way of enhancing the timing resolution in distributed quantum information processing tasks. The core of the algorithm is not limited to correlated photon pairs and applies universally to any correlation features. In particular, it is readily extended to prepare-and-measure approaches [6] that show correlations between computer-generated pulses and their time of arrival at the receiver. Our method for software-based synchronization in postprocessing can thus be implemented straightforwardly in state-of-the-art QKD systems and may pave the way toward quantum networks [53] with improved synchronization performance, as well as entirely new applications such as secure time transfer [54,55].

II. RESULTS

The following sections start with a short introduction to clocks and their impact on quantum communication scenarios. Subsequently, we describe the protocol to synchronize even poorly performing clocks by means of correlated photons and discuss its corresponding implementation. Toward the end, we summarize the findings and test the performance in an emulated free-space link experiment that includes turbulence and introduces signal fading.

A. Synchronization protocol

The performance of remote clocks used in communication networks has a great impact on the most appropriate method for their synchronization. High-performance oscillators (e.g., rubidium clocks) provide a precise frequency but also exhibit small but constant difference frequencies (or clock-frequency skew). In analogy to archery, the archer hits a spot on average, but off center (see Fig. 1). These oscillators provide high accuracy, i.e., small clock drift, as well—the frequency variation over time is small (the archer hits a targeted spot with small scatter). Both a small clock drift and clock-frequency skew are necessary to maintain low synchronization-timing jitter (the archer always hits the same spot, which corresponds to the mark). Such precise and stable references relax the

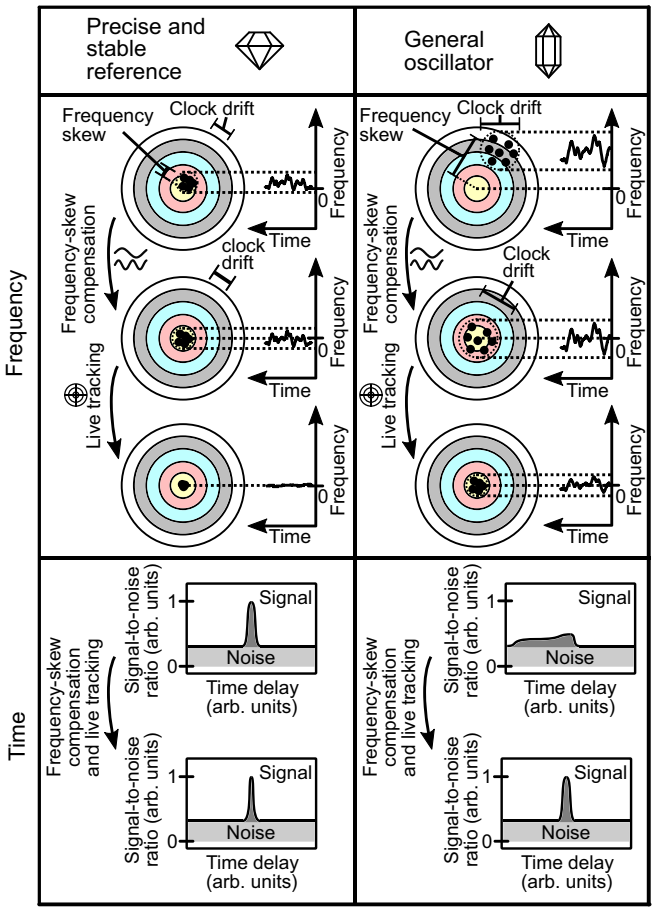

FIG. 1. The impacts of clock performance. The frequency of real imperfect clocks differs from a nominal value and varies over time. The effect is much stronger for general oscillators (e.g., quartz oscillators) than precise and stable references (e.g., rubidium clocks). The compensation of frequency skew (i.e., the frequency difference of clocks) increases the accuracy and further enhancements to the precision are made through live tracking of the clock drift (i.e., time-varying clock frequencies). The correlation peak in the time domain shows significant timing jitter and may even be asymmetric, because of strong frequency variation over time in general oscillators. Clock-frequency skew compensation and live tracking can reduce the additional timing jitter from poorly performing clocks to a minimum.

requirements on synchronization protocols and are still commonly employed in experiments [19,21,44]. The focus of the proposed work is on general oscillators, which are widely used but exhibit a frequency skew that is orders of magnitude higher. Hence, any synchronization protocol for such oscillators will rely crucially on an initial compensation of frequency skew—especially in real link scenarios with a low signal-to-noise ratio. Their strong and nonlinear drifts also make live tracking of the correlation with short feedback-loop times necessary. Furthermore, the optical-link characteristics play a crucial role, since it is the only mediator for timing information.

In our experimental implementation, we use entangled photon pairs from an untrusted source as a mediator of timing signals between distant parties [Fig. 2(a)]. Note that the feature of entanglement is neither necessary for the synchronization protocol nor does it improve the timing precision in our implementation. The photons are produced at 810 nm via type-II spontaneous parametric down-conversion with a 405-nm continuous-wave pump laser (brightness 229×10^3 counts/s/mW/nm coincidences). We select the 800 nm channel for the highest performance in free-space link experiments [14,17,19,54]. The wide spectral bandwidth of 0.4 ± 0.17 nm corresponds to a coherence length of <2.5 ps (the time-bandwidth product of Gaussian pulses) that represents small intrinsic timing jitter of single photons. The source operates in a regime of single-photon generation. Although there is a low probability of multiphoton events, it will not affect the synchronization performance, as the timing is identical.

To this end, we establish a synchronization protocol, which consists of four main steps, where each step reduces the timing uncertainty further—from coarse millisecond timing down to the picosecond level or smaller [Fig. 2(b)]. The first part of the correlation-based synchronization protocol is to align the data packages at the two receivers. The electronic time taggers generate time tags for single-photon detection events relative to their respective internal clocks. These time tags are stored on a personal computer in the form of data packages, each with an acquisition time of approximately 100 ms. To detect the photons, we employ Si single-photon avalanche-diode (SPAD) detectors with a photon-detection efficiency of approximately 60%, dark-count rates of 300 counts/s, and a rms timing jitter of approximately 140–180 ps root-mean squared. As a very first step in the initialization, we use classical network pinging through the NTP [11]. This establishes coarse millisecond synchronization and ensures that the data packages to be compared carry correlated detection events—this procedure is not part of this paper. The next step is to identify the correlation peak in these data packages. However, due to the clock-frequency skew, the position of the correlation peak is itself a function of time, which results in significant spreading of the correlation peak over the 100-ms integration time. The clock-frequency skew could be computed by observing a moving correlation peak, which is a typical chicken-and-egg problem, as it implies that the peak has already been identified [42]. This becomes especially critical in low-signal scenarios, where it is impossible to recover correlation features (for the impact of signal and clock-frequency skew on correlation peaks, see Appendix A 1). To address this issue, we introduce a coarse clock-frequency skew compensation before identifying the correlation peak with high visibility in the second step. This reduces the frequency skew of typical quartz

oscillators from approximately 20 μs/s to ≤1 μs/s and thereby reduces the spreading of the correlation peak to ≤100 ns over the typical acquisition time of 100 ms. By squeezing the correlation peak, it also enhances the signal-to-noise ratio, which makes synchronization in high-loss communication scenarios possible. In the third step, we cross-correlate the time tags of matched data packages using fast-Fourier-transform (FFT) convolution and derive the precise time difference between the master and slave, i.e., the timing offset. Optionally, we fine tune the clock-frequency skew through calculating the correlation peak over the start-stop method [56–58]: a photon arriving at Alice (Bob) starts the counter and the second photon at Bob (Alice) stops it. The collection of time differences in a histogram represents the cross-correlation. This is computationally substantially more efficient than FFTs because it considers only two subsequent and neighboring time tags [as opposed to all, in the case of FFTs; see Fig. 2(c)]. The downside of this cross-correlation method is that it requires a good initial estimate of the timing offset. Specifically, the precision of the timing offset must be smaller than the inverse single-photon count rate (for more information, see Appendix A 4). In summary, after data-package synchronization (step 1), we match the clock frequencies in step 2 and estimate the timing offset in step 3. These are the requirements for starting the quantum communication session. During a long communication session, the frequency of unstable clocks will change unpredictably. It follows a frequency mismatch between the two clocks that enormously increases the total system jitter. Live tracking of the correlation peak during the communication session and the fast feedback loops in step 4 mitigate against rapid variations of the clock frequencies.

B. Implementation of the synchronization protocol

With the basic work flow established, we now consider the major challenges associated with its implementation in real link scenarios. A low signal-to-noise ratio and

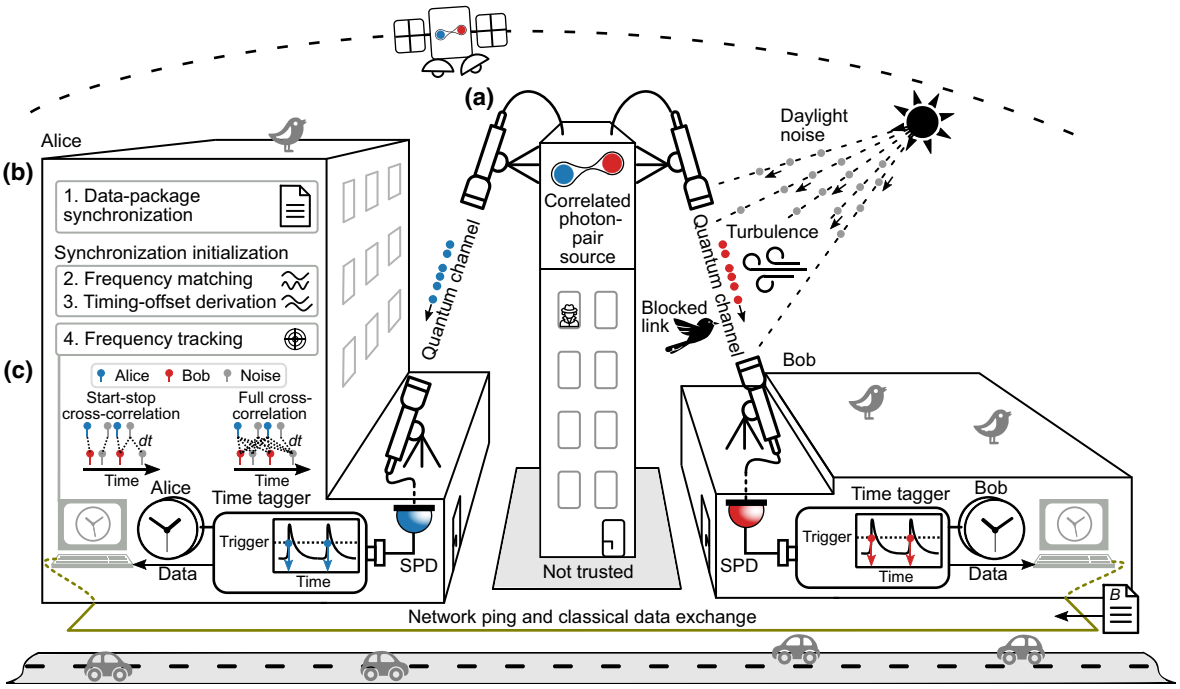

FIG. 2. A schematic of the synchronization work flow and the derivation of timing information with correlated photons. (a) The steps for synchronization include data-package synchronization, clock-frequency skew estimation, timing-offset calculation and correlation-peak tracking over fast Fourier transform (FFT) or start-stop-method-based cross-correlations. (b) Time-correlated photons induce electrical pulses on single-photon detectors (SPDs) that are time tagged when the voltage exceeds a threshold value. These correlated detection events act as mediator to synchronize the master and slave clocks of two communicating parties Alice and Bob. The clocks may be the internal quartz-crystal oscillators of the time taggers, external rubidium clocks, or GPS-disciplined clocks. The synchronization performance is compared with a local reference from Bob for varying quantum channel attenuation and emulated turbulence with Fried parameter $r_0 = 1$ mm and a beam waist of 3.4 mm ($1/e^2$) on the channel to Bob. (c) The cross-correlations are calculated through either FFTs or using a computationally efficient start-stop method. The former is crucial during initialization, when the exact timing offset between Alice and Bob is unknown, i.e., there is a given timing-offset uncertainty that is larger than the inverse single-photon rate (for more information, see Appendix A 4). Here, time differences (dt) between all time tags are included. In the start-stop method, only two subsequent time tags are considered.

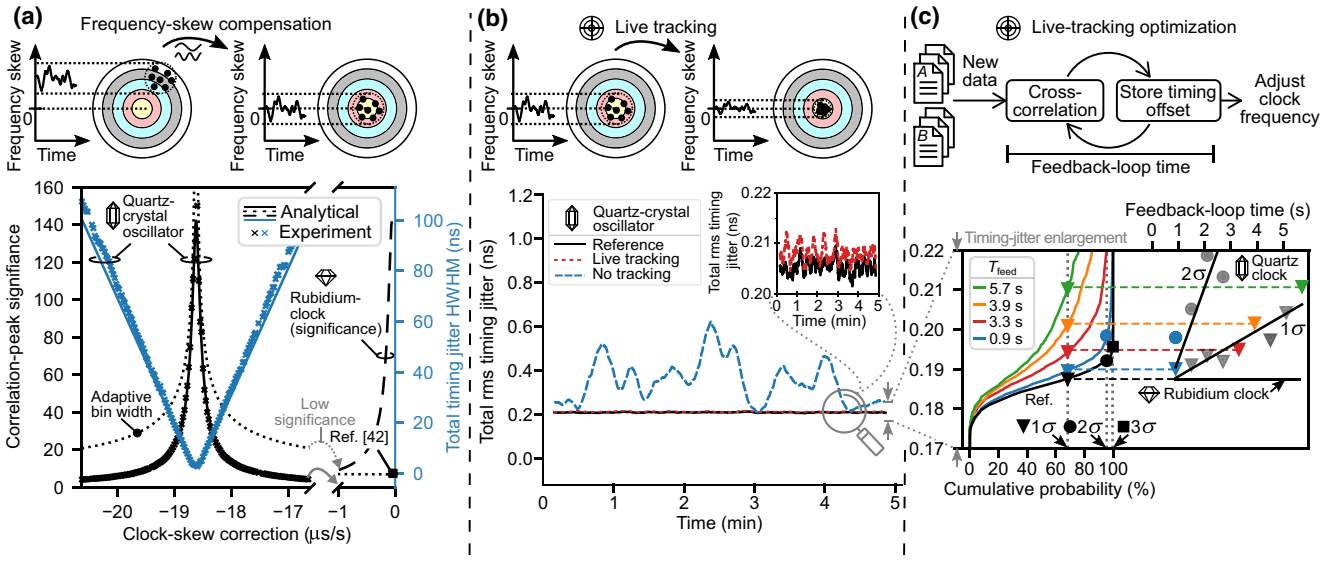

FIG. 3. Clock-frequency skew compensation and live tracking. (a) The ratio of peak height to background standard deviation (the significance) increases and the correlation-peak spread reduces for correctly compensated clock-frequency skew. Rubidium clocks do not require any compensation of the clock-frequency skew and result in strong correlation peaks. The significance can be increased by adapting the bin width to the current clock-frequency skew (see Appendix A 1). The analytical trend lines [timing jitter given in Eq. (A16) and significance given in Eq. (A17)] are derived from the experimental maximum significance of 141. This provides the smallest residual clock-frequency skew of 48 ns/s and the smallest timing jitter of 2.4 ns over the acquisition time of 0.1 s. (b) Live tracking of the correlation peak reduces the drift of the clock-frequency skew over time. The clock-frequency skew is adjusted every 600 ms in a feedback loop and this results in much smaller total timing jitter, which is almost identical to the reference with the same clocks. The synchronization-jitter contribution is as small as 35 ± 8 ps, with an acquisition time of 100 ms. The other experimental parameters are given in Appendix A 6. (c) The timing offset from the cross-correlation peak location is stored for every incoming data package up to the feedback-loop time. The instantaneous clock-frequency difference is equal to dividing the average timing offset by the elapsed time. Whereas the feedback-loop time does not affect the performance of stable rubidium oscillators much, it heavily affects the synchronization jitters achieved with quartz oscillators. Here, we characterize the performance by accumulating the occurrence probability for all jitter values during a 5-min session. The 1σ (2σ, 3σ) timing jitter represents the maximum jitter in 68.3% (95.5%, 99.7%) of the time during the session. The synchronization jitter increases linearly with the feedback-loop time [Eq. (3)]. The gray data points correspond to measurements that are not displayed in the cumulative-probability plot.

large clock-frequency skews have a severe impact during synchronization initialization (Sec. II B 1). In worst-case scenarios, it is not possible to synchronize the system, as the correlation features stay hidden beneath the noise. Initial sweeps of the clock-frequency counteract this and enable successful initialization. Having passed this first hurdle, it is easy to keep the slave-clock frequency locked to the master during the communication session. Here, we take advantage of filtering the data in time by narrowing down the observation window of correlation features. In contrast to time windows as large as the acquisition time of 100 ms during the initialization, it is narrowed down to a few tens of nanoseconds, which reduces the noise drastically. However, clock drifts create a frequency mismatch between the master and the slave clock after the initialization of synchronization procedure. This increases the timing jitter during the communication session, which in turn increases the quantum bit error rate. All of this is circumvented by tracking of the clock frequency and immediate compensation, as described in Sec. II B 2.

1. Initialization

The accumulation of simultaneous photon-detection events from matched data packages results in a correlation peak that is located at the timing offset between two communicating parties. It is a major challenge to distinguishing the correlation peak that corresponds to this offset from the noisy background. For that purpose, we introduce the statistical significance as the peak height normalized to the noisy-background standard deviation [42]. A strong spread of the correlation peak in time reduces the significance. This spread is equivalent to and characterized by the total system timing jitter, including detection, time tagging, and synchronization jitter. Typical rms timing jitters of single-photon detection systems are smaller than 500 ps and, also, time-tagging units achieve jitters smaller than a few tens of picoseconds with ease. Poor synchronization on the other hand, with its corresponding synchronization jitter, has the most severe impact on the total system jitter. It may amount to 1 μs, with an uncorrected clock-frequency skew of 20 μs/s and an acquisition time of 100 ms.

The synchronization jitter is time dependent and increases with the acquisition time T_a and the uncorrected clock-frequency skew Δu. When the clock-frequency skew or the acquisition time is sufficiently large, the distribution of the arrival time of photons is no longer Gaussian and describes a higher-order Gaussian function [see Fig. 10(b)] with a full width at half maximum equal to $\Delta u T_a$. At lower clock-frequency skews or acquisition times, the increase in the width is smaller by a factor of $\sqrt{2}$, i.e., when transitioning from a Gaussian to a higher-order Gaussian distribution. As the distribution is not necessarily normally distributed (it may even be asymmetric), we take the half width at half maximum (HWHM) instead of the rms width for a more intuitive and universal measure. In conclusion, the synchronization jitter σ_{sync} (HWHM) can be upper bounded as

$$\sigma_{\text{sync}} \leq \frac{1}{2}\Delta u T_a. \tag{1}$$

Frequency skew reduces the height of the correlation peak and thereby decreases the probability of correctly identifying it. Systems with stable oscillators, such as rubidium clocks, do not suffer from a reduction of significance [Fig. 3(a)] without correction. General crystal oscillators, on the other hand, lower the signal close to the noise level and thus make it impossible to find the correlation peak. To counteract this, we introduce compensation of the skew, so that the ith time tag on Bob's side t_i is corrected to t_i^c:

$$t_i^c = t_i - \Delta u_c\,(t_i - t_0)\,. \tag{2}$$

For different values of corrections Δu_c, we calculate the cross-correlation under the constraint of computational effort, which limits us to the computation of approximately 280 cross-correlation functions (for the algorithm and computational requirements, see Appendix A 2). This is sufficient to search in a clock-frequency skew range from -20 to $+20$ μs/s (determined according to our quartz-crystal clock). The step size of 0.14 μs/s provides clock-frequency skews with an uncertainty <0.14 μs/s. The optimum clock-frequency skew is indicated by the maximum significance of the correlation peak in the search window [Fig. 3(a)]. The maximum significance of 142 allows us to create helpful trend lines with a coincidence rate of 7×10^3 counts/s, a single rate on Alice's side of 244×10^3 counts/s, a single rate on Bob's side 232×10^3 counts/s, and an acquisition time of 0.1 s (see Appendix A 3 a). The experimental timing jitter is derived by fitting the correlation peak with a higher-order (flat-top) Gaussian function. Note that the significance is enhanced by adapting the bin size to the correlation-peak spread (see Appendix A 1) and reaches values of up to 6.8 [see Eq. (A1)] without clock-frequency skew compensation. However, the correlation-peak spread is unknown at this point in time, as the true clock frequency is uncertain. Such a random selection of the bin size reduces the significance again. In contrast to previous work [42], we could increase the significance by a factor of $\sqrt{\Delta u/\delta u} \approx 20$, due to our method of clock-frequency skew compensation. Further reduction of the residual clock-frequency skew is made by a more computationally efficient fine tuning (see Appendix A 4) or by observing moving correlation features [42]. Whereas we cannot avoid noise, clock-frequency skew compensation sharpens the correlation features and makes them more visible (more information on the signal-to-noise ratio dependence is presented in Fig. 6). This provides noise resistance and makes it feasible to initialize low signal-to-noise ratio links.

2. Live tracking

At this point in the protocol, the sender and receiver have matched clock frequencies and the corresponding timing offset. The next challenge is to maintain this common time basis over extended periods via live tracking of the correlation peak. In the case of rubidium oscillators or GPS-disciplined clocks, which do not exhibit significant clock-frequency drifts, this step is not necessary. Typical quartz oscillators, however, require the initial estimate for the clock-frequency skew to be adapted in real time. In other words, we adjust the time-varying slave-clock frequency to match the changed master-clock frequency. These drifts result in a measurable change of the position of the correlation peak. The location is continuously tracked and the slave-clock frequency is subsequently adapted by the peak displacement over the elapsed time (see detailed algorithm in Appendix A 5). In our experiment, the acquisition time is 100 ms and the feedback-loop time for adapting the instantaneous clock frequency is 600 ms. Figure 3(b) compares the total timing jitter with and without live tracking to Bob's reference that indicates zero-synchronization jitter (for the single-count rate, see Appendix A 6). Over a time window of 5 min, we find maximum clock-frequency-skew variations of up to ± 11 ns/s, which shows the importance of live correcting these clock drifts of 320 ps/s^2 (see Appendix A 7). Without live tracking, the timing jitter would increase from 200 ps to almost 700 ps with a 100-ms acquisition time. This is not the case when applying our live-tracking algorithms. Smaller clock drifts or fast feedback-loop times would provide even better performance. Stable frequency references (here, rubidium clocks) show particularly small clock drifts and introduce very low timing jitters of smaller than 1 ps as a consequence of live tracking (see Appendix A 5). Quartz oscillators require more rigorous treatment and optimization of the algorithms. With a stronger drift of the clock, $\partial(\Delta u)/\partial t$, a timing jitter of σ_{sync} is introduced [see Eq. (1)], with a longer feedback-loop time T_{feed} and acquisition time T_a:

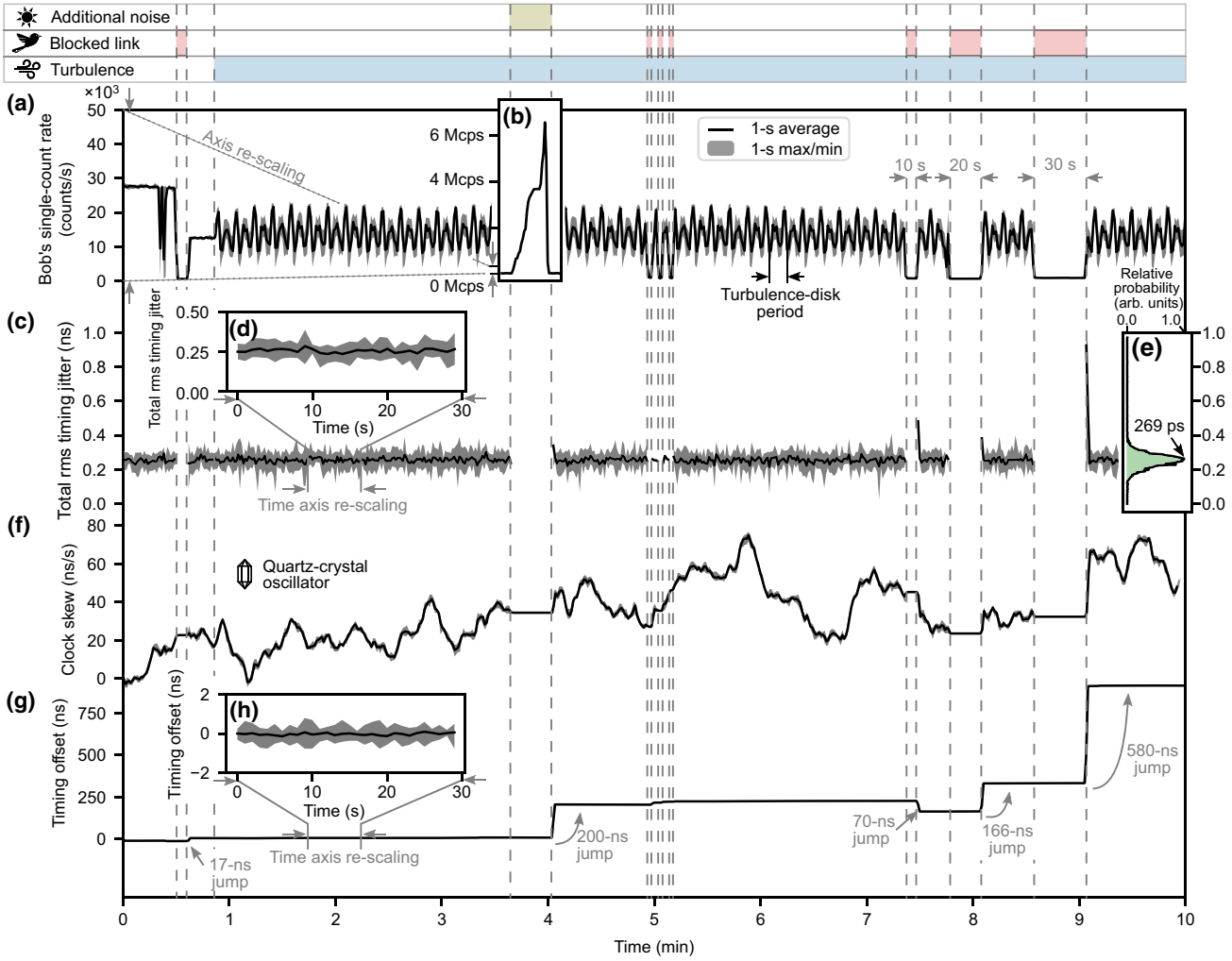

FIG. 4. The in-laboratory emulated free-space link experiment. At different times, we add additional noise at Bob's receiver, block the optical link, or add turbulence (Fried parameter 1 mm, $1/e^2$ full-width beam waist of 3.4 mm). (a) The single-count rate at the receiver, Bob. The mean single-count rate is $(15 \pm 5) \times 10^3$ counts/s, with a coincidence rate of 440 ± 200 counts/s (the coincidence window is equal to a rms timing jitter of 269 ps) in the time window from minute 1 to minute 3.5. Alice's count rate lies constantly at $(195 \pm 3) \times 10^3$ counts/s. (b) The introduction of a noise source increases Bob's count rate to 6×10^6 counts/s. A low signal-to-noise ratio stops the correlation-peak tracking and keeps the instantaneous clock-frequency skew for correction constant. (c),(d) The time-dependent total rms timing jitter (c) remains constant (d) even after switching on the turbulence at minute 1. (e) The timing-jitter probability distribution describes a Gaussian with its fitted center at 268.7 ± 0.7 ps (minute 1 to minute 3.5). Setups with the same clock (perfect synchronization) show timing jitters of 260 ± 2 ps from a fit to 10 s of data acquisition, estimating the rms synchronization jitter to 68 ± 8 ps. (f) The tracking algorithm is stopped in regions with low signal-to-noise ratios (blocked optical link or additional noise) and in those regions results in constant clock-frequency skew for correction. (g) The timing offset jumps after low signal-to-noise ratio time intervals, as the correlation peak is not tracked and the clock frequency is not adapted. This phenomenon is stronger for a longer duration of blocked links. (h) The timing offset varies within a window of ± 1 ns on time scales of 30 s. The feedback-loop time and data-package size amount to 200 ms and 100 ms, respectively. A summary of this figure is presented in Table I.

$$\sigma_{\text{sync}} \leq \frac{1}{2} T_a \int_0^{T_{\text{feed}}} \frac{\partial(\Delta u)}{\partial t} dt. \tag{3}$$

Large feedback-loop times do not compensate the rapidly changing clock frequencies early enough and result in a linear increase of the overall timing jitter [Fig. 3(c)]. The increase of timing jitter with respect to the feedback-loop time is a measure of the clock drift. Quartz oscillators indicate a much stronger increase of the timing jitter with the feedback-loop time than ultrastable rubidium clocks. The total feedback-loop time is affected by electrical devices, such as single-photon detectors or the time-tagging units that introduce time delays. However, their impact is negligible in comparison to slow classical communication or time-tag processing, which are major

TABLE I. The residual root-mean-square (rms) synchronization jitter for different link rates and coincidence to-accidentals ratios (CARs) during live tracking. With regard to the synchronization initialization, see Fig. 7 for comparison of the different setups. The clocks are external crystal oscillators (XOs) or clocks locked by the Global Navigation Satellite System (GNSS). (a) The low-signal experiment, including satellite up-link turbulence (see Appendix A 8). (b) The moderate-signal experiment, including satellite up-link turbulence (Fig. 4). (c) The 1.2-km free-space and high-dimensional link experiment across Vienna by Steinlechner *et al.* [19]—synchronization jitter estimated from timing-offset variation. (d) The 143-km free-space link experiment between the La Palma and Tenerife in the Canary Islands by Ecker *et al.* [21]—synchronization jitter estimated from timing-offset variation. The coincidence window (half width) depends on the detection system and is as follows: (a),(b) 0.27 ns; (c) 1 ns; (d) 0.5 ns.

Parameter	(a) Low signal	(b) Moderate signal	(c) 1.2-km link, Vienna	(d) 143-km link, Canary islands
Clock type	External XO	External XO	GNSS	GNSS
Alice's count rate ($\times 10^3$ counts/s)	165 ± 3	195 ± 3	400	13 300
Bob's count rate ($\times 10^3$ counts/s)	437 ± 6	15 ± 5	100	10
Correlation-event rate (counts/s)	430 ± 160	440 ± 200	20 000	>300
CAR	10 ± 4	84 ± 13	250	<5
Rms synchronization jitter (ps)	98 ± 6[a]	68 ± 8	≈ 33	≈ 50
Rms clock drift (ps/s^2)	320	320	<5 (typical)	<5 (typical)
Clock-frequency skew (parts per million, ppm)	19	19	10^{-6} (typical)	10^{-6} (typical)

[a]Only live tracking—synchronization initialization at stronger signal.

drivers. A low signal and other link conditions reduce the synchronization quality further. This is discussed in Sec. II C.

C. Experiment under emulated link conditions

To confirm the feasibility of our approach in real-world link conditions, we perform a series of experiments with added background noise and signal fades, as is expected in free-space links with atmospheric turbulence. To this end, we emulate several link scenarios and introduce turbulence via a rotating phase plate, designed to represent an atmospheric uplink to a satellite from the Mt. Teide optical ground station (Fried parameter 1 mm, with $1/e^2$ full-width beam waist of 3.4 mm [50]). This turbulence results in strong variations of Bob's detected count rate [Fig. 4(a)]. The rate at Alice, who is assumed to be colocated with the quantum source, remains constant. To test the stability of the algorithm under elevated noise levels (e.g., stray light), we introduce background counts via a light-emitting diode [see Fig. 4(b)]. Even under these unfavorable conditions, live tracking with short feedback loops (200 ms) ensures rms synchronization-timing jitters of 68 ± 8. This is comparable to 50-ps synchronization jitter from systems with GPS-disciplined clocks [21]. Our timing jitter is estimated with the same-clock rms timing jitter of 260 ± 2 ps and the average timing jitter of 268.7 ± 0.7 ps after a Gaussian fit to the jitter values from minute 1 to minute 3.5 [Figs. 4(c)–4(e)]. The correlation-peak tracking algorithm stops when it reaches a signal-to-noise ratio threshold that is set to 5. The setting of a threshold is required, as it avoids noise being wrongly identified as a correlation feature. Both the increased noise and interruptions of the optical link (e.g., due to objects crossing the beam path) stop the tracking, as the signal-to-noise threshold is not reached, and leave the instantaneous clock-frequency-skew constant [Fig. 4(f)]. This only impacts very lossy links with a rms synchronization-timing jitter increased to 98 ps, as described in Appendix A 8. When the clock-frequency skew for correction is not adapted in low-signal regions, the correlation peak will start to move in time. As a consequence, the timing offset jumps to the value of the current location, as soon as the signal is back. Long periods of lost signal follow in large timing-offset jumps and depend on the stability of the clock. These timing-offset jumps are unique to unstable clocks. They require sufficiently large observation windows in order not to lose the correlation peak that is essential for synchronization. The timing offset is bound to fluctuations in a window of ± 1 ns [Figs. 4(g) and 4(h)] in good signal conditions (coincidence-to-accidentals ratio >5). In Appendix A 8, we present stable live tracking for much lower coincidence-to-accidentals ratios of only 10 (Table I), comparable to high-loss link scenarios [21]. The rms synchronization-timing jitter amounts to 98 ± 6 ps, with only 43 correlation events in a 100-ms data package and a 200-ms feedback-loop time. Note that the correlation-peak significance during synchronization initialization is extremely low with the rates given, similar to Ref. [21] (for a comparison of different setups in the literature, see Fig. 7). Our synchronization-initialization algorithms fail here, due to limited computation time and power that cannot compensate the clock-frequency skew enough for sufficient significant correlation features. Therefore, we increase the signal-to-noise ratio during initialization and reduce it again later. In conclusion, the combination of (a) an adaptive correlation observation window,

(b) the introduction of a coincidence-to-accidentals ratio threshold, and (c) short feedback-loop times enables very stable operation and only a minor increase of the total timing jitters.

III. DISCUSSION

These results clearly show that the compensation of clock-frequency skew and live tracking of the frequency are suitable for application in a variety of real-world link scenarios. We could show that very few correlation events are already sufficient to establish and keep a synchronized quantum communication session with timing jitter in the range of tens of picoseconds over time scales of 10 min. Recently, we have also confirmed these results on a 1.7-km intracity link. Reference [42] predicts that a sufficient significance of greater than 7 can only be achieved by clock-frequency skews of <1.3 μs/s in our realistic link experiment [Table I(b) and Eq. (A1)]. This means that the synchronization initialization would fail, as our clock-frequency skew amounts to 18.5 μs/s (for a comparison of different setups from other publications, see Fig. 7). This is a consequence of the poor visibility of the correlation peak. Furthermore, previous treatments have been limited to high signal-to-noise ratios. Here, we demonstrate successful synchronization for much lower signal-to-noise ratios due to compensation with an effective frequency skew of less than 48 ns/s, which enables the enhancement of the significance by a factor of 20 as part of the initialization [Fig. 3(a)]. This brings correlated photons and quartz oscillators into a much better position—not only for today's typical quantum communication schemes [19] but also for tomorrow's long-distance and low-signal scenarios. The intrinsic timing relations of correlated photons clearly have the potential to replace bulky external high-precision synchronization schemes and move resources from hardware to software.

Finding the timing offset is crucial in order to start communication, but a low signal-to-noise ratio will reduce the correlation-peak significance. Especially high-loss scenarios of >46.9 dB [21] [Table I(d)] call for very low clock-frequency differences for sufficient visibility of the correlation-peak. This typically requires highly precise oscillators, such as rubidium or GPS-disciplined clocks. Quartz clocks are acceptable in principle, but demand a precise slave-clock frequency sweep to achieve a frequency match with the master. Within our presented search window of -20 μs/s to $+20$ μs/s, it is impossible to find this precise frequency to the required accuracy of <14 ns/s. High computation times give rise to limitations (see Appendix A 2). The solution is prior knowledge of the approximate clock frequencies to narrow down the search window—ideally, just a single initial cross-correlation will be necessary in order to find the correlation peak. We propose to minimize the search window by (a) more accurate frequency specifications from the clock manufacturer, (b) the calibration of clocks with high signal rates, or (c) finding the clock frequency at a time when the computational limits are not a constraint. The use of high-performance computers with high parallel-processing speeds—e.g., with a graphical processing unit—also reduces the computation time. Note that finding the initial clock-frequency skew is a single-time issue, as it will not occur during high-duty quantum communication sessions. The algorithm tracks the aging of the clocks and adjusts the clock frequency continuously. Starting with a large frequency uncertainty, the estimations improve over time. This provides a narrow clock-frequency search range before every session, where the computational effort is reduced drastically, down to a few seconds—even for lossy long-distance links.

Systems with very high losses or accelerating clocks suffer from increased synchronization jitter during communication. A low number of correlation events increases the uncertainty of the clock-frequency skew for compensation and unlocks live-tracking feedback loops. Low clock stability further increases the synchronization-timing jitter. High-precision clocks clearly have an advantage here that allows for much lower synchronization jitters <1 ps during communication sessions, due to low drifts through their high stability. Apart from the signal-to-noise ratio and the clock stability, detector jitter is another factor for high synchronization performance. In particular, high-loss scenarios benefit from low detection jitters that increase the signal-to-noise ratio. We demonstrate that even 44 correlation events in 100-ms data packages are sufficient for a synchronization jitter of a few tens of picoseconds. The event rate and the signal-to-noise ratios are comparable to extremely high-loss scenarios [21] [Table I(d)] but are enough to enable correlation-peak tracking and keep the system locked. As nanowire detectors already have timing jitters of as low as tens of picoseconds, the synchronization performance with correlated photons will only increase in future.

To set our approach into a broader perspective, we also briefly discuss limits to moving objects, such as satellite- [14,15] or emerging drone-based [59,60] quantum communication. Quantum sources in space provide a great platform to test and measure space-time effects on quantum communication protocols [61,62] or perform high-precision metrology [63,64]. Satellites introduce an effective clock-frequency skew due to the Doppler effect caused by the varying distance to the observer. The normalized Doppler shift $\vec{v}\,(t)/c$ for low-Earth-orbit satellites increases from 0 to 2×10^{-5} over a time scale of 6 min, where $\vec{v}\,(t)$ is the time-dependent relative velocity of the satellite and c is the speed of light [65]. Equivalently, this creates a clock-frequency skew that varies from 0 to a maximum of $\Delta u = 20$ μs/s. Whereas the maximum

clock-frequency skew is comparable to our crystal oscillator, the clock acceleration $\partial(\Delta u)/\partial t$ is orders of magnitude larger and amounts to approximately 55 ns/s^2 (20 μs/s divided by 6 min). Thus, it is desirable to reduce the feedback and acquisition time to 100 ms or smaller, which could result in clock-drift jitters of 265 ps [Eq. (3)]. However, with only a few correlation events per second available [14,66], it is impossible to choose acquisition times of <1 s and still have a sufficient signal-to-noise ratio. Using only correlated photons, synchronization is not possible without knowledge of the orbit of the satellite. Sources with 10^3-counts/s rates [54], on the other hand, provide the opportunity to select small feedback cycles of 100 ms and still have correlation events comparable to those of our experiment [Table I(b)], which could be used to synchronize clocks by means of our method. Drones move much slower than satellites and may also be suitable for synchronization—at least classically [67]. Their speed is up to 30 m/s, introducing clock-frequency skews of up to 100 ns/s (30 m/s divided by the speed of light), this being much smaller than the clock-frequency skew of our crystal oscillators. The main concern is acceleration of the drone, which can reach up to 7*g* (gravitational constant) and can translate to a clock drift of 228 ns/s^2. Sufficient 10^3-counts/s coincidence rates [59] provide the opportunity to select short feedback cycles for the compensation of high drifts during drone acceleration and make synchronization feasible. With small feedback loops, correlation events open doors for live remote detection of the velocity and acceleration of moving objects.

Several research initiatives are bringing the technical complexity of correlated photon-pair sources close to those of pulsing laser diodes for synchronization. The photon-pair source can already be designed on a compact footprint (on chip) and comes with an interface to optical fiber [68,69]. In essence, the major building blocks are just a continuous-wave laser as the optical pump and a fiber-coupled nonlinear crystal (commercially available) requiring only active stabilization of the temperature. Fortunately, the stabilization challenge comes with a much higher intrinsic timing precision that is a few picoseconds (in this paper) but can be extended to femtoseconds [70,71], due to the availability of a high spectral bandwidth of several tens of nanometers. This easily exceeds the timing precision of pulsed laser diodes [54], which are also known from the White Rabbit protocol (a precision network-time protocol), where a synchronization performance of better than 100 ps is reached [72]. Much higher precision is classically only achievable with complex stabilized cavities for ultrashort-pulse generation [73] or frequency combs [74,75]. Furthermore, correlated photons are attractive, as nonclassical effects can be used. This includes the Hong-Ou-Mandel effect to improve the timing resolution [36,76] or the effect of nonlocal dispersion compensation [33,77] for dispersion robustness.

IV. CONCLUSIONS

Correlated photons are great timing carriers, adapt to quantum communication systems naturally, and are easy to recycle for high-performance synchronization down to a few tens of picoseconds. The method of finding correlation signatures is independent of the source type and also applies to pulsed single-photon sources that indicate correlations between the time of the sent photons and time of arrival at the receiver. Today's point-to-point or laboratory-to-laboratory communication sessions will be integrated into a network with multiple users tomorrow, as can be found in action already [10]. Our technique can be extended to several parties by source modifications to, e.g., the multiphoton entanglement. The communicating parties make decisions about a master clock that shares its time tags with all the other parties and allow for the adjustment of their slave clocks. High scalability, integration, and fewer resources characterize the networks, where highly stable but bulky clocks should be an exception. Whereas correlated photons used to be considered inappropriate for synchronizing clocks with high skew and strong drifts [42], we show stable operation by means of our proposed synchronization methods. Clock-frequency skew compensation and correlation-peak live tracking allow for a wider range of cases—especially in terms of scalability. Hereby, the clock feedback signal is suited not only for postprocessing time-tag information but can be used for active adjustment of optical components (e.g., fiber stretchers) as well. We show resistance to high losses, as would be common in large networks, and still achieve rms synchronization-timing jitters of <68 ps. This suggests feasibility for application in real-life communication scenarios. Single photons are not copyable and bit errors during communication are easy to detect due to the quantum origin of the single-photon detection events [6,7], indicating, furthermore, the potential for quantum secured time transfer [54,55,78].

The data that support the findings of this study are available from the corresponding author upon reasonable request.

ACKNOWLEDGMENTS

C.S., M.C.P., and A.K. are part of the Max Planck School of Photonics, supported by the German Federal Ministry of Education and Research (BMBF), the Max Planck Society, and the Fraunhofer Society. This research was conducted within the scope of the project QuNET, funded by the BMBF in the context of the federal government's research framework in IT security "Digital. Secure. Sovereign." The authors declare no conflicts of interest.

APPENDIX A: METHODS

1. Correlation-peak significance and comparison to previous work

The peak significance S_p of the correlation features reduces with high clock-frequency differences Δu, as described in Ref. [42],

$$S_p = \sqrt{\frac{r_C^2 N}{r_A r_B}} = \sqrt{\frac{r_C^2}{r_A r_B \Delta u}}, \tag{A1}$$

with coincidence (or signal) count rates of r_C and single rates of r_A from Alice and r_B from Bob. This, however, only considers the situation in which the bin width $\delta t = T_a/N$, with the number of bins N, has been perfectly adapted to the spread of the correlation peak δt_{spread} over the acquisition time T_a,

$$\delta t_{\text{spread}} = T_a \Delta u. \tag{A2}$$

The clock-frequency skew Δu is not known usually, so that it will be hard to guess the bin size correctly. This results in a reduction of significance by $\sqrt{N}$ for bin widths that are too large [Eq. (A1)]. Similarly, if the bin width is too small, the signal will be distributed over several bins. The number of coincidences per bin will reduce according to the ratio $\delta t_{\text{spread}}/\delta t$,

$$S(N) = \frac{1}{\Delta u N}\sqrt{\frac{r_C^2 N}{r_A r_B}}, \tag{A3}$$

where $\Delta u N \geq 1$. Figure 5(a) depicts this behavior for the photon-pair source from Ref. [42]. In their work, with their high signal-to-noise ratio, it is possible to find the very first correlation peak and determine the clock-frequency skew from the correlation-peak displacement over time. In this paper, we test lower signal-to-noise ratios that would result in a significance of barely 2.5 with a clock-frequency skew of $\Delta u = 2 \times 10^{-4}$ [Fig. 5(b)]. As a consequence, it would not even be possible to start with the algorithms as described in Ref. [42]. In this work, we propose a clock-frequency skew compensation for this crucial initial step in low signal-to-noise environments. We find that improvements of the clock-frequency-skew uncertainty by a factor of 140 are feasible, depending on the FFT run times (for the computational requirements, see Appendix A 2). This provides an improvement of the significance by a factor of $\sqrt{140} \approx 12$, to a value close to 30, and enables reliable identification of the correlation peak even under low signal-to-noise ratios. Note that we reduce the residual clock-frequency skew to $\delta u = 48$ ns/s (with the rate given and its final peak significance) that even provides a significance improvement by a factor of 20.

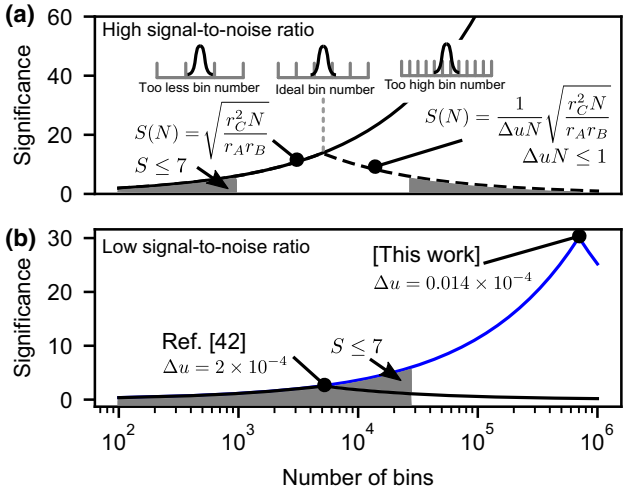

FIG. 5. A comparison of Ref. [42] and this work. (a) Time tags are recorded over the acquisition time and sorted into a number of bins that impact the significance. The value of significance refers to the ratio of signal to the standard deviation of the noise [Eq. (A1)]. With single-count rates of $r_A = r_B \approx 77 \times 10^3$ counts/s, signal rates of $r_C \approx 15 \times 10^3$ counts/s, and a clock-frequency skew of $\Delta u = 2 \times 10^{-4}$, the significance reaches 13—sufficient for synchronization initialization. (b) The methods of Ref. [42] fail for lower signal-to noise ratios, $r_A = 200 \times 10^3$ counts/s, $r_B = 800 \times 10^3$ counts/s, and $r_C = 14 \times 10^3$ counts/s, as the correlation peak cannot be found due to the low significance of 2.5. Here, we introduce compensation of the clock-frequency skew that provides a better guess of the clock-frequency skew, following in higher significance by the square root of the number of cross-correlations in the clock-frequency skew search (here, there is a factor-of-12 improvement).

More detailed relations between the significance and the signal-to-noise ratio are depicted in Fig. 6. Starting from single-count rates on Alice's (r_A) and Bob's (r_B) side, Bob's single rate reduces as the link transmission T reduces by means of a variable attenuator. Furthermore, this similarly reduces the coincidence rate r_C. Following Refs. [79–81], the coincidence-to-accidentals ratio (CAR) is defined as the number of true coincidence counts r_{CTrue} over the accidental coincidence counts r_{CAcc}:

$$\text{CAR} = \frac{r_{\text{CTrue}}}{r_{\text{CAcc}}} = \frac{r_C - r_{\text{CAcc}}}{r_{\text{CAcc}}}. \tag{A4}$$

The number accidental correlation events r_{CAcc} depend on the link transmission T and on the rms coincidence window σ, as

$$r_{\text{CAcc}}(T) = 2 r_A \left[(r_B - r_{\text{back}})T + r_{\text{back}}\right]\sigma. \tag{A5}$$

Here, we also introduce the background rate r_{back}, which cannot be reduced further by higher channel losses. This includes factors such as detector dark counts, insufficiently

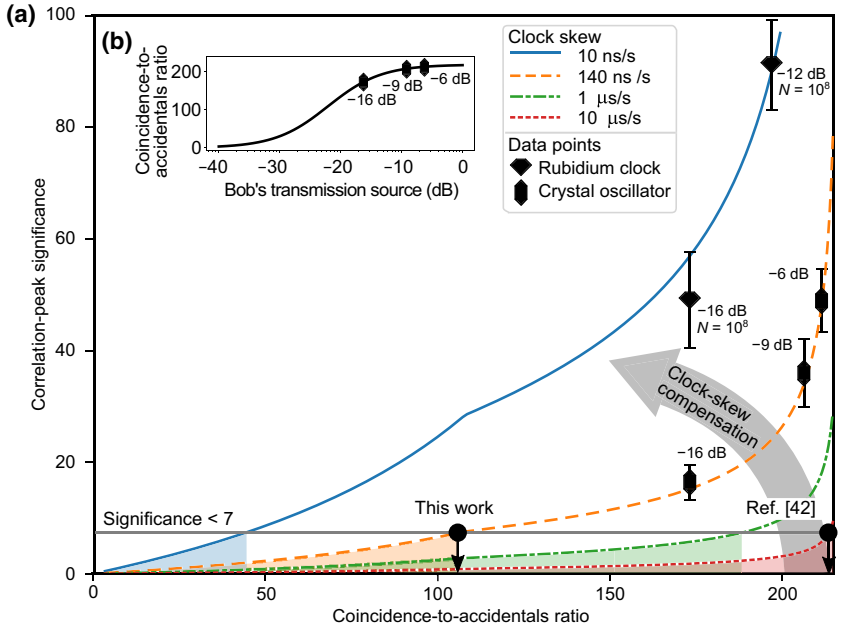

FIG. 6. The correlation-peak significance for different loss scenarios. (a) An estimation of the correlation-peak significance under different coincidence-to-accidentals ratios (loss) and clock-frequency skews Δu. The experimental data points are based on initial lossless rates of $R_A = 200 \times 10^3$ counts/s, $R_B = 800 \times 10^3$ counts/s, $R_C = 14 \times 10^3$ counts/s, and $r_{\text{back}} = 5 \times 10^3$ counts/s and a maximum number of bins in the cross-correlation of $N = 10^8$. The number of bins is adapted to the correlation-peak spread, caused by the residual clock-frequency skew, with $\Delta u = 1/N$. The error bars indicate the standard deviation after slight variation of the bin sizes by ±5%. The threshold for recovering the correlation peak is a significance of 7, providing a probability of approximately 10^{-12} of a wrongly found peak [42]. The clock-frequency skew compensation increases the visibility of the correlation peak and thus enables higher noise resistance in this work. (b) The coincidence-to-accidentals ratio, which depends on the transmission from Alice to Bob [see Eq. (A6)].

filtered daylight, or other noise sources in the system. The transmission-dependent CAR is summarized as

$$\text{CAR}(T) = \frac{r_C T - 2r_A\left[(r_B - r_{\text{back}})T + r_{\text{back}}\right]\sigma}{2r_A\left[(r_B - r_{\text{back}})T + r_{\text{back}}\right]\sigma}. \quad \text{(A6)}$$

The transmission-dependent peak significance can be derived from Eq. (A1) as

$$S_p(T) = \sqrt{\frac{(r_C T)^2}{r_A\left[(r_B - r_{\text{back}})T + r_{\text{back}}\right]\Delta u}}. \quad \text{(A7)}$$

The analytical trend, as described by Eq. (A7), is confirmed experimentally (Fig. 6) after compensation of the clock-frequency skew by different amounts. The peak significance is achieved by matching the cross-correlation bin size with the peak spread from the residual clock-frequency skew, as described earlier. However, for clock-frequency skews smaller than 10 ns/s, the number of bins is already $N = 1/(10 \times 10^{-9}) = 10^8$, which results in immense computational effort (more information is given in Appendix A 2). It is hardly feasible to adapt the bin size to its optimum for clock-frequency skews of $\leq$10 ns/s. It follows a nonoptimized cross-correlation that does not provide maximum significance. Nevertheless, Fig. 6 shows impressively how the significance of the correlation peaks can be increased by compensation of the clock-frequency skew.

Reduction of the clock-frequency skew by our algorithm can help to recover the correlation features under very low signal-to-noise ratios. High signal rates do not demand any kind of compensation. On the other hand, this is crucial in high-loss link scenarios (Fig. 7, with data from Table I). Here, we are limited to a clock-frequency skew compensation of 140 ns/s, which allows for synchronization initialization of our emulated link experiment [see Fig. 4 and Table I(b)]. Even lower rates, as in Appendix A 8 [see Table I(a)] or in Ref. [21], cause too small correlation-peak significance for synchronization initialization today (Fig. 7). Higher correlation-peak significance is expected to be reached by means of more computational power or reduction of the clock-frequency-skew search window.

2. Synchronization-initialization algorithms and computational effort

The correlation peak is found by a convolution of the time-tag streams from Alice and Bob. Without precise knowledge of the clock-frequency skew, it will be difficult to find correlation peaks with sufficient significance.

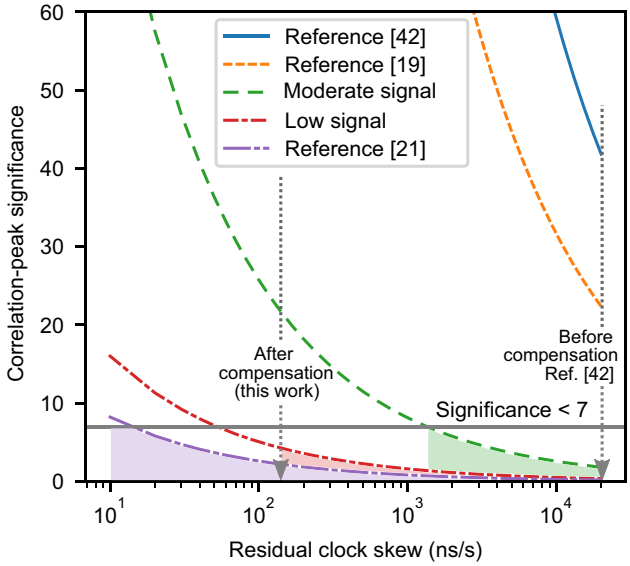

FIG. 7. The correlation-peak significance for various experimental setups. The clock-frequency skew of the quartz oscillator is up to 20 µs/s, providing the clock-frequency skew before compensation. Even without compensation, it is easy to find the correlation peaks with sufficient signal, as in Refs. [42] and [19]. The threshold for recovering the correlation peak is a significance of 7, giving a probability of approximately 10^{-12} of a wrongly found peak [42]. Low coincidence-to-accidentals ratios, as in our low-signal [Appendix A 8 and Table I(a)] or moderate-signal experiment [Fig. 4 and Table I(b)] or in Ref. [21], require compensation of the clock-frequency skew. With our limited computational power, we can reduce and compensate the clock-frequency skew to <140 ns/s. This is not sufficient to reach a significance of 7 in our low-signal experiment or in Ref. [21]. The solution would be to reduce the initial clock-frequency-skew search window.

Input: time tags Alice t_A and Bob t_B
Functions: READ TIME TAGS(), CONVOLUTION(), SLEEP()
Output: optimum clock-frequency skew

SLEEP(integration time = 0.1 s)
t_A, t_B = READ TIME TAGS()
skew vector = -20 µs/s $\cdots + 20$ µs/s, step: 140 ns/s
bins = 0 . . . 0.1 s, step: 14 ns
P = zeros(skew-vector size)
$i = 0$
for Δu_{corr} ***in*** skew-vector **do**
  $t_{B_{\mathrm{corr}}} = t_B + (t_B - t_B[0]) \times \Delta u_{\mathrm{corr}}$
  c = CONVOLUTION$(t_A, t_{B_{\mathrm{corr}}}, \mathrm{bins})$
  $P[i] = \max(c)$
  $i+ = 1$
end
optimum clock-frequency skew =
 skew-vector(argmax(P))

ALGORITHM 1. Representations of the functions COARSE CLOCK-FREQUENCY SKEW() and ACCURATE CLOCK-FREQUENCY SKEW() in Fig. 11. The convolutions are FFT based and start-stop method based, respectively. A FFT-based approach has to be taken if the precise timing offset is not known. The algorithm includes the following variables: time tags from Alice and Bob $t_{A/B}$, peak values of the cross-correlations P, counter i, clock-frequency skew for correction Δu_{corr}, clock-skew correct time tags from Bob $t_{B_{\mathrm{corr}}}$, and cross-correlation output c. Note that the bin step size of 14 ns corresponds to an integration-time × skew-vector step size. Smaller bin and skew-vector step sizes require considerably higher computational effort. If there is knowledge of the approximate clock-frequency skew, the range of clock-frequency skews can be reduced.

First, the clock-frequency-skew search window is created (Algorithm 1). From our quartz oscillator data sheet, we know the approximate range of clock-frequency skews, starting from −20 to +20 µs/s (see Appendix A 7). The time tags from Bob are compensated by different clock-frequency skews every loop analogous to Eq. (2) and then convoluted with time tags from Alice. It is either based on the FFT, in the case of determining the clock-frequency skew coarsely [Fig. 3(a)], without knowledge of the timing offset, or on the start-stop method. In the case of the FFT, it is necessary to assign the time tags to the bins and then apply the cross-correlation. In the start-stop method, the time differences are binned after the correlation.

Full cross-correlations over all time tags are time consuming and limit the feasible number of calculations. The correlations are performed through a PYTHON) environment with the NumPy module on a personal computer (Table II). The time for a single FFT-based cross-correlation may amount to up to approximately 40 s for $N = 10^7$ bins [Fig. 8(a)]. The optimum significance is reached by choosing a sufficient number of bins, N, such that the correlation-peak spread is equal to the bin size (see Appendix A 1). This yields the achievable clock-frequency-skew accuracy δu:

$$\delta u = \frac{1}{N}. \tag{A8}$$

The total computation time T_{tot} from a single cross-correlation $T(\delta u)$ for a range of clock-frequency skews ΔU

TABLE II. The personal-computer specifications for calculating the FFT.

Parameter	Value
Processor	Intel® Core™ i5-8250U CPU
Speed	1.60 GHz (1.80 GHz)
RAM	16 GB
System	64-bit-based processor
Environment	PYTHON 3.7.0 64 bit, NumPy 1.19.4

is then

$$T_{\text{tot}} = \frac{\Delta U}{\delta u} \times T(\delta u). \tag{A9}$$

With a time limit of slightly above 2 h (7500 s) and a clock-frequency-skew range of $\Delta U = 40$ μs/s (from −20 to +20 μs/s), the maximum affordable time for a single cross-correlation is approximately 26 s and clock-frequency-skew accuracy is 0.14 μs/s ($N = 7.14 \times 10^6$). The speed of 26 s for a single cross-correlation may be drastically increased by using a dedicated higher-performing computer, instead of a laptop in this work. More specifically, more processing cores and a higher processing speed could improve the situation. Graphical processing units may also perform much better by parallelization of the processes and FOR loops.

3. Estimation of synchronization jitter and trend lines

a. Description of total system jitter

The total system jitter of a quantum communication system determines the overall performance—from the signal-to-noise ratio to the secure bit rate. The total jitter can be easily calculated analytically with knowledge of the clock-frequency skew. Here, we provide important scaling laws to estimate the final signal-to-noise ratios, such as the significance or the coincidence-to-accidentals ratio. As all jitter contributions originate from a random source, we consider a Gaussian function g with rms jitter σ that is normalized to have an area of 1:

$$g(t) = \frac{1}{\sqrt{2\pi\sigma^2}} \exp\left(-\frac{t^2}{2\sigma^2}\right). \tag{A10}$$

The total jitter from the source coherence time σ_{coh}, time tagger σ_{tt}, detector σ_{det}, and synchronization σ_{sync},

$$\sigma = \sqrt{\sigma_{\text{coh}}^2 + \sigma_{\text{tt}}^2 + \sigma_{\text{det}}^2 + \sigma_{\text{sync}}^2}, \tag{A11}$$

reduces to

$$\sigma \approx \sqrt{\sigma_{\text{det}}^2 + \sigma_{\text{sync}}^2} \tag{A12}$$

as the jitter contribution from the time tagger (around 30 ps rms) and the entangled-photon-source coherence time (around 2.5 ps rms) is much smaller than the detector jitter. After a few steps of editing, we obtain

$$\sigma = \sigma_{\text{det}} \sqrt{1 + \frac{\sigma_{\text{sync}}^2}{\sigma_{\text{det}}^2}}, \tag{A13}$$

resulting in the simulated jitter curves shown in Fig. 3(a). Due to the residual clock-frequency skew after compensation, the smallest jitter is not equal to the detector jitter.

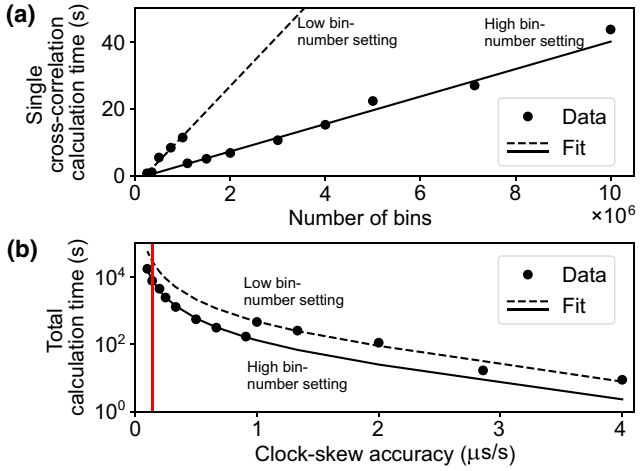

FIG. 8. The FFT computation times for different clock-frequency-skew accuracies. (a) The single-cross-correlation computation time depending on the number of bins. The personal computer (Table II) uses two different settings for calculations, depending on the number of bins. In case of adaption of the bin width to the correlation-peak spread, the clock-frequency-skew accuracy is equal to the inverse of the number of bins [Eq. (A8)]. (b) The total computation time for a search window of −20 μs/s to +20 μs/s with a given clock-frequency-skew accuracy (step size).

The highest correlation-peak value P (replaceable by the coincidence-to-accidentals ratio CAR or the significance S), given by the smallest timing jitter σ_{min}, is reduced due to the stronger synchronization jitter. Using Eq. (A12), the correlation-peak value is described as

$$P = \frac{P_0}{\sqrt{1 + \left(2\sigma_{\text{sync}}/\sqrt{2\pi}\sigma_{\text{min}}\right)^2}}. \tag{A14}$$

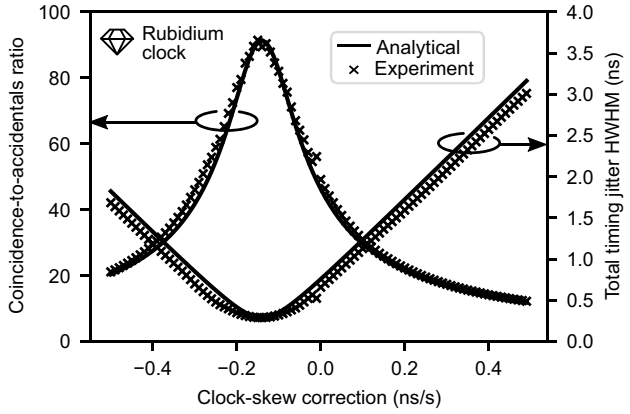

FIG. 9. The coincidence-to-accidentals ratio and total timing jitter (HWHM) for the corrected clock-frequency skew of rubidium oscillators. The smooth trend indicates a stable reference. The analytical trend lines are derived from the experimental acquisition time of $T_a = 10$ s, the smallest timing jitter of 320 ps, and the maximum coincidence-to-accidentals ratio of 91.

The prefactor of $\sqrt{2/\pi}$ originates from the area of a Gaussian being equal to $\sqrt{2\pi}\sigma$ and its change of shape to a flat-top Gaussian by the synchronization jitter. Figure 9 indicates a smooth trend of CAR and the total rms timing jitter for rubidium clocks. The smallest experimental timing jitter amounts to $\sigma_{\min} = 310$ ps, with a maximum coincidence-to-accidentals ratio CAR_0 of 91 and an acquisition time T_a of 10 s. Together, both enable an analytical trend line from Equations 1, A13, and A14 with acquisition time $T_a = 10$ s (Fig. 9):

$$\mathrm{CAR}(\Delta u) = \frac{\mathrm{CAR}_0}{\sqrt{1 + (2/\pi)\left[(1/2\Delta u T_a/\sigma_{\min})\right]^2}}, \quad \text{(A15)}$$

$$\sigma(\Delta u) = \sigma_{\min}\sqrt{1 + \left(\frac{1/2\Delta u T_a}{\sigma_{\min}}\right)^2}. \quad \text{(A16)}$$

Equation (A14) may also be transformed to be dependent on the residual clock-frequency skew Δu and the smallest residual clock-frequency skew δu, as the smallest timing jitter $\sigma_{\min}$ and smallest residual clock-frequency skew δu are directly related through Eq. (1),

$$S(\Delta u, S_p) = \frac{S_p}{\sqrt{1 + (2/\pi)\left(\Delta u/\delta u(S_p)\right)^2}}, \quad \text{(A17)}$$

with the smallest residual clock-frequency skew δu defined by Ref. [42]:

$$\delta u(S_p) = \frac{r_C^2}{r_A r_B S_p^2}. \quad \text{(A18)}$$

The maximum significance of 142 allows us to create helpful trend lines with a coincidence rate of $r_C = 7 \times 10^3$ counts/s, a single rate on Alice's side of $r_A = 244 \times 10^3$ counts/s, a single rate on Bob's side of $2r_B = 232 \times 10^3$ counts/s, and an acquisition time of 0.1 s (see Appendix A 3 a). The analytical trend of the significance is derived directly from the maximum experimental significance S_p and follows Eq. (A17). The smallest residual clock-frequency skew at peak significance can be calculated simultaneously as $\delta u = 48$ ns/s with $S_p = 142$ [see Eq. (A18)] and leads to the smallest timing jitter $\sigma_{\min} = 2.4$ ns with Eq. (1). Furthermore, the peak significance S_p enables analytical trend lines of the total timing jitter σ as $\sigma^2 = \sigma_{\min}^2 + \sigma_{\mathrm{sync}}^2$, providing a close match with the experimental timing jitters [Fig. 3(a)].

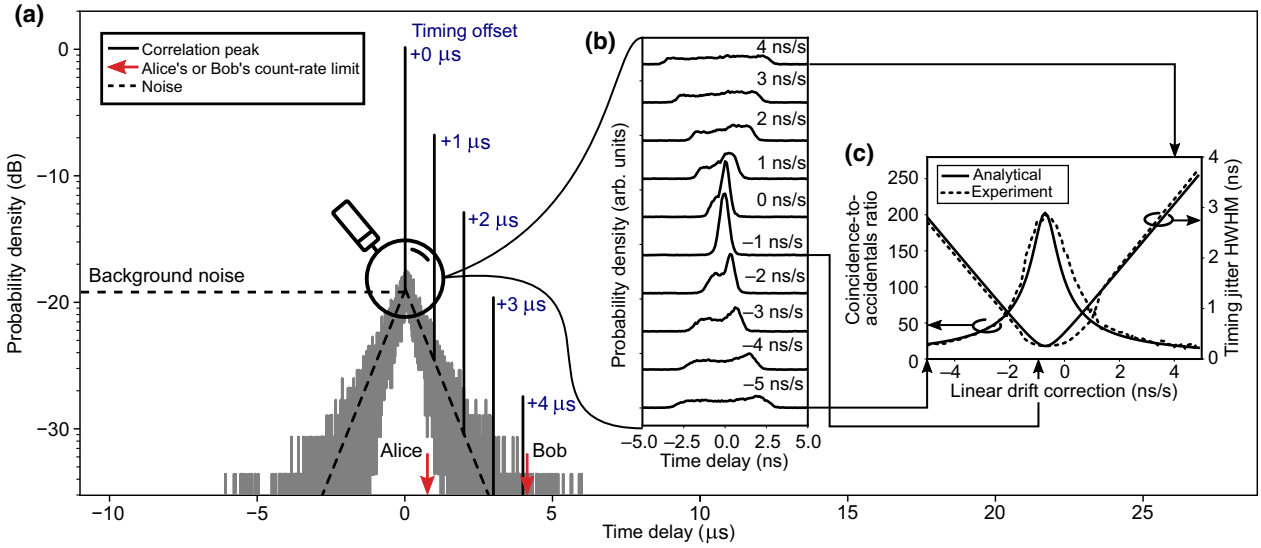

FIG. 10. Fine tuning of clock-frequency skew through cross-correlation with the start-stop method. (a) Correlation peaks for various timing-offset accuracies. The noise values are highest at small time delay with −20 dB and reduce exponentially until the inverse count rate at Bob is approximately reached. The peak noise level is larger than the correlation peak for poor timing-offset precision >2.5 µs. Peak-search algorithms may still recover the peak here, instead of a simple search for a maximum at the timing-offset precision <2.5 µs. (b) An enlarged view of the timing-offset-corrected cross-correlation peaks for various clock-frequency skew-compensation values. The shape of the correlation peaks depends on the compensated clock-frequency skew and may be asymmetric due to clock instabilities. (c) The correlation-peak coincidence-to-accidentals ratio or its timing jitter (HWHM) is an ideal indicator of the optimum clock-frequency skew compensation, as they become maximum and minimum, respectively. The analytical trend lines are derived from the experimental acquisition time of 1.4 s, the smallest timing jitter of 258 ps, and the maximum coincidence-to-accidentals ratio of 204.

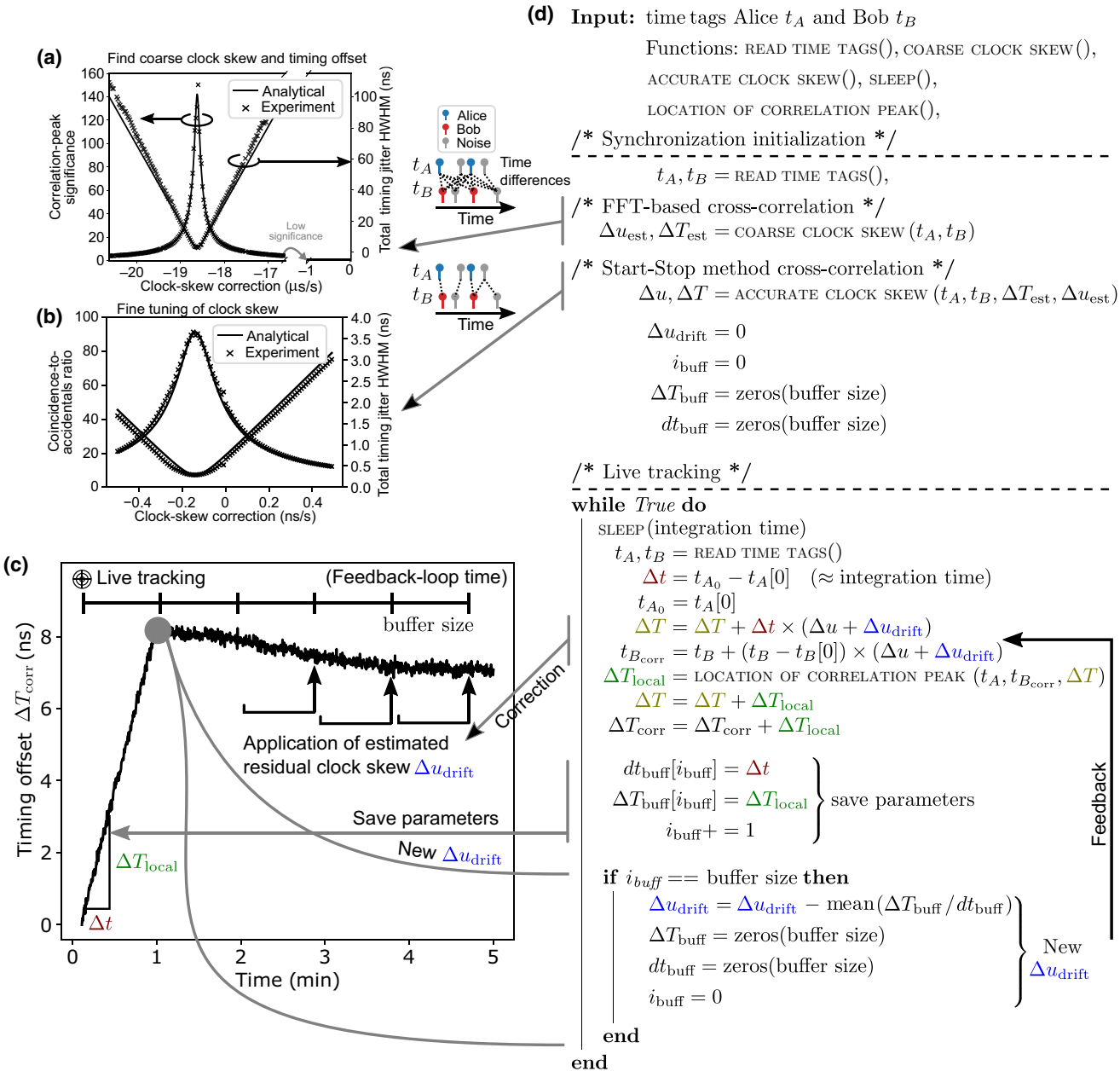

FIG. 11. The initialization and live-tracking algorithm. (a) A coarse search of the clock-frequency skew. (b) Fine tuning of the clock-frequency skew. (c) Estimation of the residual clock-frequency skew over a feedback time of approximately 1 min with two rubidium clocks. The residual clock-frequency skew over the last 4 min amounts to 6.4 ps/s, resulting in synchronization jitters of approximately 0.32 ps over an acquisition time of 100 ms. (d) The algorithm for synchronization initialization and live tracking includes the following variables: time tags from Alice and Bob, $t_{A/B}$; first estimated clock-frequency skew, Δu_{est}; estimated timing offset, ΔT_{est}; accurate timing offset, ΔT; clock-frequency skew, Δu; instantaneous clock-frequency skew from clock drifts, $\Delta u_{\mathrm{drift}}$; buffer of local timing offset, ΔT_{buff}; buffer of local time difference, dt_{buff}; buffer counter, i_{buff}; time difference, Δt; time of previous sample, t_{A_0}; clock-skew corrected time tags from Bob, $t_{B_{\mathrm{corr}}}$; local timing offset, $\Delta T_{\mathrm{local}}$. The location of the correlation peak is found through an efficient start-stop cross-correlation.

b. Achievable synchronization-timing jitter during live tracking

The final synchronization jitter after live correction during a communication session is determined by the clock drift and the number of correlation events. Here, we present analytical estimations of the synchronization limits that might be helpful for easy transfer to any communication scenario. The most important parameter is the instantaneous clock-frequency skew during a communication session. If it is nonzero, due to insufficient

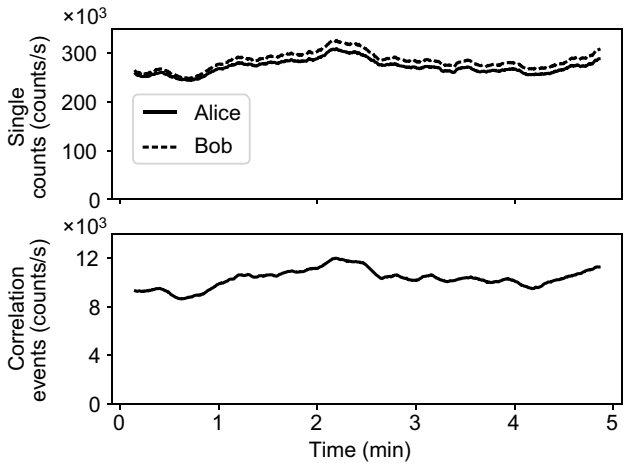

FIG. 12. Photon-pair rates according to the experiment in Fig. 3(b).

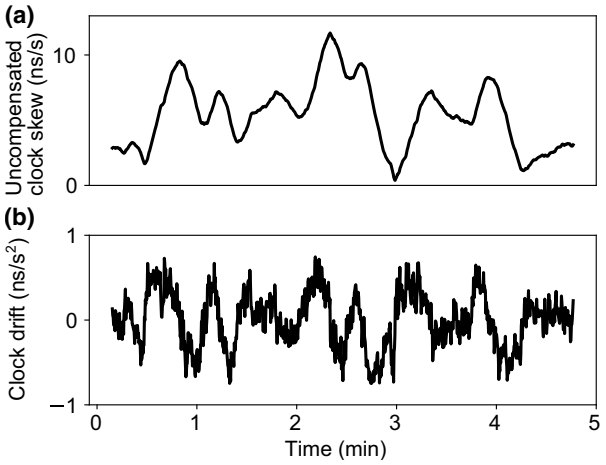

FIG. 13. (a) The instantaneous clock-frequency skew Δu drifts without live tracking. (b) The time-dependent clock drift $\partial(\Delta u)/\partial t$ is zero on average, with a standard deviation of 320 ps/s^2.

correction, the synchronization jitter will be nonzero. The clock-frequency skew Δu is calculated from two or more detected peak locations, τ_1 and τ_2, with a temporal separation of T_{meas}:

$$\Delta u = \frac{\tau_2 - \tau_1}{T_{\text{meas}}}. \tag{A19}$$

However, low numbers n of correlation events give rise to an uncertainty in the correlation-peak location $\delta\tau$ via the total timing jitter σ [42]:

$$\delta\tau = \frac{\sigma}{\sqrt{n-1}}. \tag{A20}$$

Via error propagation, we obtain the uncertainty of the clock-frequency skew from measurement, Δu_{meas}:

$$\Delta u_{\text{meas}} = \sqrt{2}\frac{\delta\tau}{T_{\text{meas}}}. \tag{A21}$$

Together with Eqs. (1) and (A20), the coincidence rate r_C, and the acquisition time T_a, the synchronization jitter due to the uncertainty in the peak position measurement is

$$\sigma_{\text{meas}} = \frac{1}{2}\sqrt{2}\frac{\sigma}{\sqrt{r_C T_a - 1}T_{\text{meas}}}T_a. \tag{A22}$$

The second jitter contribution comes from the clock drift $\partial(\Delta u)/\partial t$. Clock-frequency skew that has not been foreseen previously may accumulate over the feedback-loop time T_{feed}:

$$\Delta u_{\text{drift}} = \int_0^{T_{\text{feed}}} \frac{\partial(\Delta u)}{\partial t} dt. \tag{A23}$$

Together with Eq. (1), the resulting synchronization jitter, due to the drifting clock, is

$$\sigma_{\text{drift}} = \frac{1}{2}T_a \int_0^{T_{\text{feed}}} \frac{\partial(\Delta u)}{\partial t} dt. \tag{A24}$$

Both the measurement and the synchronization jitter limit the total achievable synchronization jitter during live tracking [Fig. 3(c)]:

$$\sigma_{\text{sync}}^2 = \sigma_{\text{meas}}^2 + \sigma_{\text{drift}}^2. \tag{A25}$$

4. Clock-frequency-skew fine tuning and start-stop method

Careful fine tuning of the optimum clock-frequency skew for compensation reduces the synchronization jitter to a minimum. As the timing offset is calculated with nanosecond accuracy in the synchronization initialization, it is feasible to shrink the observation window down to $<$100 ns to reduce the computational effort. The cross-correlations are now derived by the computationally efficient start-stop method [56–58]. In contrast to the FFT cross-correlation, which correlates all time tags from Alice with all time tags from Bob, the start-stop method calculates time differences between neighboring time tags. If the timing offset is not calculated with a precision smaller than $\text{Min}\{1/r_A, 1/r_B\}$, this increases the probability of wrongly calculated time differences and thus reduces the number of correlation events. The correlation-peak height reduces and finally becomes smaller than the peak noise values [Fig. 3(a)]. The correlation peak compresses to the smallest width $\sigma_{\text{min}} = 258$ ps by compensation of the residual clock-frequency skew. In addition, the coincidence-to accidentals ratio reaches its maximum of $\text{CAR}_0 = 204$ over a

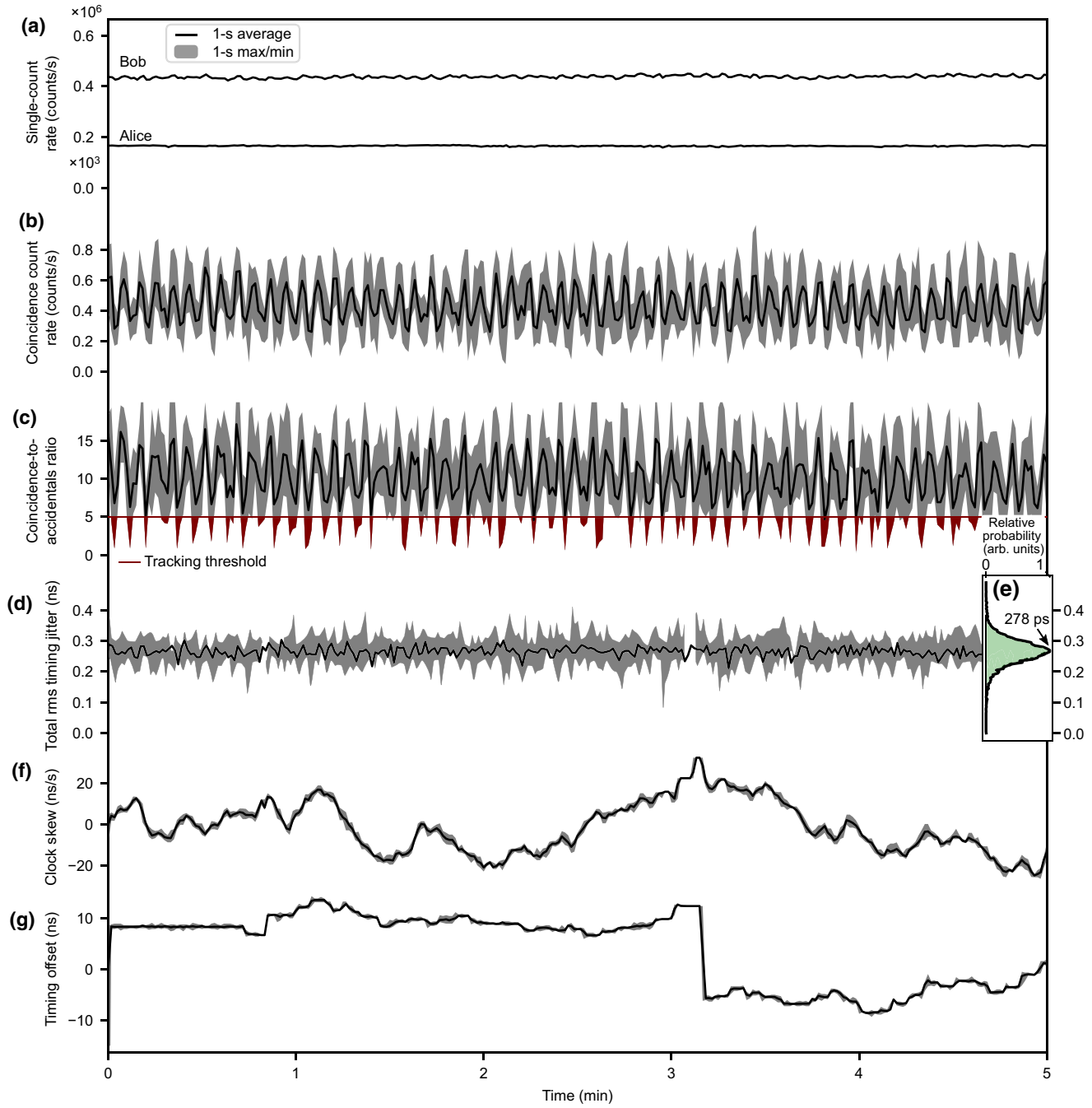

FIG. 14. The low-correlation-rate live tracking under turbulence. Turbulence parameters: Fried parameter 1 mm, $1/e^2$ full-width beam waist of 3.4 mm. (a) The count rate at the receiver (Bob) of $437 \pm 6 \times 10^3$ counts/s is increased artificially by a noise source. Alice's count rate amounts to $165 \pm 3 \times 10^3$ counts/s. (b) The average coincidence rate is 430 ± 160 counts/s (the coincidence window is equal to a rms timing jitter of 267 ps) and indicates periodic fluctuations from the turbulence disk. (c) The mean coincidence-to-accidentals ratio is 10 ± 4, with a correlation-peak live-tracking threshold of 5. The evolution of the total timing jitter (d) is described by a Gaussian probability distribution with its fitted center at 277.8 ± 0.8 ps (e). Together with same-clock total timing jitter of 260 ± 2 ps, the synchronization jitter is approximately 98 ± 6 ps. (f) The tracked clock-frequency skew displayed over time. (g) The timing offset varies more than in a high-signal environment (Fig. 4), because of partially stopped tracking when the coincidence-to-accidentals ratio falls below 5. This gives rise to an increase of the total timing jitter. The feedback-loop time and data-package size amount to 200 ms and 100 ms, respectively. A summary of this figure is presented in Table I.

coincidence window that is determined by the total timing jitter. The experimental correlation peak is fitted by a stretched Gaussian function and then the timing jitter is derived from it. The experimental total jitter and peak value behave perfectly as given analytically (see Appendix A 3 a). Clocks with high stability, i.e., a constant frequency difference between two clocks, create a jitter envelope with a plateau. Rubidium oscillators are known for their high stability of 10^{-12} over 1 s [82,83] and create a jitter envelope with a plateau, as the frequency difference is almost constant over time. Quartz-crystal oscillators, on the other hand, may show weak stability of only 10^{-11} to 10^{-9} over 1 s [45], which results in asymmetry and gives rise to deviations between the analytical and experimental trends in a region between -1 and 2 ns/s. The method for compensation of the clock-frequency skew by a simple peak search [Fig. 3(c)] may be carried out with arbitrary resolution. Step sizes of <1 ns/s work very well to start live tracking of clock drifts in the last step of synchronization.

5. Live-tracking algorithm

After synchronization initialization, including the coarse clock-frequency-skew search [Fig. 11(a)] and its fine tuning [Fig. 11(b)], residual and time-dependent clock-frequency skews increase the synchronization jitter and call for compensation during communication sessions. Figure 11(c) presents the effect of correct compensation for rubidium clocks by the algorithm in Fig. 11(d). The correlation-peak timing offset is tracked over n data points. Any change in the timing offset would be caused by an instantaneous drift. Here, the timing offset changes by approximately 8 ns in 1 min. By applying the measured residual clock-frequency skew to future time tags, we can reduce the timing-offset change and, subsequently, the synchronization jitter. Long averaging times work especially well for highly stable clocks, such as rubidium clocks. The timing offset changes by less than 1.5 ns over 4 min after the first correction, already providing residual clock-frequency skews of <6.4 ps/s and thus synchronization jitters <0.32 ps in typical 100-ms data-package sizes without difficulty.

6. Photon-pair rates

The experimentally detected photon-pair rates determine the achievable signal-to-noise ratios and limit the synchronization jitter under high losses. Figure 12 presents the rates from the experiment [Fig. 3(b)].

7. Experimental clock drift

Knowledge of the clock stability provides important measures about the limiting synchronization jitters. To estimate the clock stability, we first compare the timing jitter without tracking to the reference [Fig. 4(b)]. Any increase from the reference is caused by synchronization jitters through the residual clock-frequency skews Δu [Eq. (1)]. The residual uncompensated clock-frequency skew is plotted in Fig. 13(a) and amounts to more than 10 ns/s. Almost ideal synchronization may be achieved if the residual clock-frequency skew is constant. However, crystal oscillators may have time-dependent frequencies that result in variation of the residual clock-frequency skew. Figure 13(b) indicates the acceleration of the clocks with time with a mean value of zero and standard deviation of 320 ps/s^2. High clock drifts require small feedback times for compensation that simultaneously demands many correlation events.

The time taggers are equipped with external crystal oscillators without temperature control. The data-sheet accuracy is ± 20 ppm, the aging is ± 3 ppm in the first year and ± 1 ppm per year of the following years. The temperature dependence is ± 0.125 ppm (25–85°C). Rubidium clocks are temperature controlled, with an accuracy of $\pm 10^{-4}$ ppm (ambient temperature 0–40°C) and aging of $<5 \times 10^{-5}$ ppm per month and the stability over 1 s is 10^{-5} ppm.

8. Low-signal live tracking

At very low signal-to-noise ratios, live tracking is still possible, even for a CAR 10 ± 4 that is close to a long-distance link between the Canary Islands (140 km) [21]. In such cases, the CAR is below the tracking threshold of 5 sometimes, which follows in a lost frequency reference, i.e. the tracking is no longer possible (Fig. 14). However, since this happens only for short times, this results in only small frequency differences between the clocks that slightly increases the rms synchronization timing jitter to 98 ± 6 ps. In contrast to live tracking, the initialization of the clock synchronization is very difficult here without knowing the approximate clock frequency. The initialization would not be possible when the normalized frequency is uncertain in a range of $-20 \ldots +20\,\mu$s/s ($1\,\mu$s/s $= 1$ ppm), as typical for crystal oscillators. In this case, it is required to narrow the search range with the help of previous measurement sessions or to initiate with a better signal-to-noise ratio.

[1] J. C. Bellamy, Digital network synchronization, IEEE Commun. Magn. **33**, 70 (1995).
[2] L. Narula and T. E. Humphreys, Requirements for secure clock synchronization, IEEE J. Sel. Top. Signal Process. **12**, 749 (2018).
[3] A. G. Phadke, *et al.*, Synchronized sampling and phasor measurements for relaying and control, IEEE Trans. Power Delivery **9**, 442 (1994).
[4] J. J. Angel*, When finance meets physics: The impact of the speed of light on financial markets and their regulation, Financial Rev. **49**, 271 (2014).

[5] J. C. Corbett, *et al.*, SPANNER: Google's globally distributed database, ACM Trans. Comput. Syst. **31**, 1 (2013).

[6] C. H. Bennett and G. Brassard, Quantum cryptography: Public key distribution and coin tossing, Theor. Comput. Sci. **560**, 7 (2014).

[7] A. K. Ekert, Quantum Cryptography Based on Bell's Theorem, Phys. Rev. Lett. **67**, 661 (1991).

[8] T. E. Northup and R. Blatt, Quantum information transfer using photons, Nat. Photonics **8**, 356 (2014).

[9] N. Gisin and R. Thew, Quantum communication, Nat. Photonics **1**, 165 (2007).

[10] Y.-A. Chen, *et al.*, An integrated space-to-ground quantum communication network over 4600 km, Nature **589**, 214 (2021).

[11] D. L. Mills, *Computer Network Time Synchronization: The Network Time Protocol on Earth and in Space* (CRC Press, Boca Raton, Florida, 2011), 2nd ed.

[12] P. Berceau, M. Taylor, J. Kahn, and L. Hollberg, Space-time reference with an optical link, Class. Quantum Gravity **33**, 135007 (2016).

[13] A. Tomita, K.-I. Yoshino, Y. Nambu, A. Tajima, A. Tanaka, S. Takahashi, W. Maeda, S. Miki, Z. Wang, M. Fujiwara, and M. Sasaki, High speed quantum key distribution system, Opt. Fiber Technol. **16**, 55 (2010).

[14] J. Yin, *et al.*, Entanglement-based secure quantum cryptography over 1120 km, Nature **582**, 501 (2020).

[15] S.-K. Liao, *et al.*, Satellite-to-ground quantum key distribution, Nature **549**, 43 (2017).

[16] S. Wengerowsky, S. K. Joshi, F. Steinlechner, J. R. Zichi, B. Liu, T. Scheidl, S. M. Dobrovolskiy, R. van der Molen, J. W. N. Los, V. Zwiller, M. A. M. Versteegh, A. Mura, D. Calonico, M. Inguscio, A. Zeilinger, A. Xuereb, and R. Ursin, Passively stable distribution of polarisation entanglement over 192 km of deployed optical fibre, npj Quantum Inf. **6**, 012307 (2020).

[17] I. Marcikic, A. Lamas-Linares, and C. Kurtsiefer, Free-space quantum key distribution with entangled photons, Appl. Phys. Lett. **89**, 101122 (2006).

[18] Y. Shi, S. Moe Thar, H. S. Poh, J. A. Grieve, C. Kurtsiefer, and A. Ling, Stable polarization entanglement based quantum key distribution over a deployed metropolitan fiber, Appl. Phys. Lett. **117**, 124002 (2020).

[19] F. Steinlechner, S. Ecker, M. Fink, B. Liu, J. Bavaresco, M. Huber, T. Scheidl, and R. Ursin, Distribution of high-dimensional entanglement via an intra-city free-space link, Nat. Commun. **8**, 15971 (2017).

[20] R. Ursin, F. Tiefenbacher, T. Schmitt-Manderbach, H. Weier, T. Scheidl, M. Lindenthal, B. Blauensteiner, T. Jennewein, J. Perdigues, P. Trojek, B. Ömer, M. Fürst, M. Meyenburg, J. Rarity, Z. Sodnik, C. Barbieri, H. Weinfurter, and A. Zeilinger, Entanglement-based quantum communication over 144 km, Nat. Phys. **3**, 481 (2007).

[21] S. Ecker, B. Liu, J. Handsteiner, M. Fink, D. Rauch, F. Steinlechner, T. Scheidl, A. Zeilinger, and R. Ursin, Strategies for achieving high key rates in satellite-based QKD, npj Quantum Inf. **7**, 5 (2021).

[22] E. F. Dierikx, A. E. Wallin, T. Fordell, J. Myyry, P. Koponen, M. Merimaa, T. J. Pinkert, J. C. J. Koelemeij, H. Z. Peek, and R. Smets, White Rabbit precision time protocol on long-distance fiber links, IEEE Trans. Ultrason. Ferroelectr. Freq. Control **63**, 945 (2016).

[23] M. Wahl, T. Röhlicke, S. Kulisch, S. Rohilla, B. Krämer, and A. C. Hocke, Photon arrival time tagging with many channels, sub-nanosecond deadtime, very high throughput, and fiber optic remote synchronization, Rev. Sci. Instrum. **91**, 013108 (2020).

[24] E. Diamanti, H.-K. Lo, B. Qi, and Z. Yuan, Practical challenges in quantum key distribution, npj Quantum Inf. **2**, 16025 (2016).

[25] D. K. L. Oi, A. Ling, G. Vallone, P. Villoresi, S. Greenland, E. Kerr, M. Macdonald, H. Weinfurter, H. Kuiper, E. Charbon, and R. Ursin, Cubesat quantum communications mission, EPJ Quantum Technol. **4**, 1 (2017).

[26] E. Kerstel, A. Gardelein, M. Barthelemy, M. Fink, S. K. Joshi, and R. Ursin, and The CSUG Team, Nanobob: A Cubesat mission concept for quantum communication experiments in an uplink configuration, EPJ Quantum Technol. **5**, 6 (2018).

[27] J.-G. Ren, *et al.*, Ground-to-satellite quantum teleportation, Nature **549**, 70 (2017).

[28] R. Valivarthi, M. G. Puigibert, Q. Zhou, G. H. Aguilar, V. B. Verma, F. Marsili, M. D. Shaw, S. W. Nam, D. Oblak, and W. Tittel, Quantum teleportation across a metropolitan fibre network, Nat. Photonics **10**, 676 (2016).

[29] Y. Tsujimoto, M. Tanaka, N. Iwasaki, R. Ikuta, S. Miki, T. Yamashita, H. Terai, T. Yamamoto, M. Koashi, and N. Imoto, High-fidelity entanglement swapping and generation of three-qubit GHZ state using asynchronous telecom photon pair sources, Sci. Rep. **8**, 1446 (2018).

[30] J.-W. Pan, D. Bouwmeester, H. Weinfurter, and A. Zeilinger, Experimental Entanglement Swapping: Entangling Photons That Never Interacted, Phys. Rev. Lett. **80**, 3891 (1998).

[31] R. Jozsa, D. S. Abrams, J. P. Dowling, and C. P. Williams, Quantum Clock Synchronization Based on Shared Prior Entanglement, Phys. Rev. Lett. **85**, 2010 (2000).

[32] I. L. Chuang, Quantum Algorithm for Distributed Clock Synchronization, Phys. Rev. Lett. **85**, 2006 (2000).

[33] V. Giovannetti, S. Lloyd, L. Maccone, and F. N. Wong, Clock Synchronization with Dispersion Cancellation, Phys. Rev. Lett. **87**, 117902 (2001).

[34] M. Krčo and P. Paul, Quantum clock synchronization: Multiparty protocol, Phys. Rev. A **66**, 024305 (2002).

[35] X. Kong, T. Xin, S.-J. Wei, B. Wang, Y. Wang, K. Li, and G.-L. Long, Demonstration of multiparty quantum clock synchronization, Quantum Inf. Process. **17**, 297 (2018).

[36] V. Giovannetti, S. Lloyd, and L. Maccone, Quantum-enhanced positioning and clock synchronization, Nature **412**, 417 (2001).

[37] R. Quan, R. Dong, X. Xiang, B. Li, T. Liu, and S. Zhang, High-precision nonlocal temporal correlation identification of entangled photon pairs for quantum clock synchronization, Rev. Sci. Instrum. **91**, 123109 (2020).

[38] R. Quan, Y. Zhai, M. Wang, F. Hou, S. Wang, X. Xiang, T. Liu, S. Zhang, and R. Dong, Demonstration of quantum synchronization based on second-order quantum coherence of entangled photons, Sci. Rep. **6**, 30453 (2016).

[39] R. Quan, R. Dong, Y. Zhai, F. Hou, X. Xiang, H. Zhou, C. Lv, Z. Wang, L. You, T. Liu, and S. Zhang, Simulation and realization of a second-order quantum-interference-based quantum clock synchronization at the femtosecond level, Opt. Lett. **44**, 614 (2019).

[40] V. D'Auria, B. Fedrici, L. A. Ngah, F. Kaiser, L. Labonté, O. Alibart, and S. Tanzilli, A universal, plug-and-play synchronisation scheme for practical quantum networks, npj Quantum Inf. **6**, 1023 (2020).

[41] A. Valencia, G. Scarcelli, and Y. Shih, Distant clock synchronization using entangled photon pairs, Appl. Phys. Lett. **85**, 2655 (2004).

[42] C. Ho, A. Lamas-Linares, and C. Kurtsiefer, Clock synchronization by remote detection of correlated photon pairs, New J. Phys. **11**, 045011 (2009).

[43] Y.-P. Yao, T.-Y. Zhang, R.-G. Wan, and W. Zhao, in *Photonics and Optoelectronics Meetings (POEM) 2011: Optoelectronic Sensing and Imaging*, edited by P. Galarneau, X. Liu, and P. Li, SPIE Proceedings (SPIE, Wuhan, China, 2012), p. 833202.

[44] J. Lee, L. Shen, A. Cerè, J. Troupe, A. Lamas-Linares, and C. Kurtsiefer, Symmetrical clock synchronization with time-correlated photon pairs, Appl. Phys. Lett. **114**, 101102 (2019).

[45] F. Tirado-Andrés and A. Araujo, Performance of clock sources and their influence on time synchronization in wireless sensor networks, Int. J. Distrib. Sens. Netw. **15** (2019).

[46] S. Bregni, Clock stability characterization and measurement in telecommunications, IEEE Trans. Instrum. Meas. **46**, 1284 (1997).

[47] C. Agnesi, M. Avesani, L. Calderaro, A. Stanco, G. Foletto, M. Zahidy, A. Scriminich, F. Vedovato, G. Vallone, and P. Villoresi, Simple quantum key distribution with qubit-based synchronization and a self-compensating polarization encoder, Optica **7**, 284 (2020).

[48] L. Calderaro, A. Stanco, C. Agnesi, M. Avesani, D. Dequal, P. Villoresi, and G. Vallone, Fast and Simple Qubit-Based Synchronization for Quantum Key Distribution, Phys. Rev. Appl. **13**, 054041 (2020).

[49] J. Williams, M. Suchara, T. Zhong, H. Qiao, R. Kettimuthu, and R. Fukumori, in *Quantum Computing, Communication, and Simulation*, edited by P. R. Hemmer and A. L. Migdall (SPIE OPTO, 2021), p. 5.

[50] B. García-Lorenzo, A. Eff-Darwich, J. J. Fuensalida, and J. Castro-Almazán, Adaptive optics parameters connection to wind speed at the Teide observatory: Corrigendum, Mon. Not. R. Astron. Soc. **414**, 801 (2011).

[51] V. Scarani, H. Bechmann-Pasquinucci, N. J. Cerf, M. Dušek, N. Lütkenhaus, and M. Peev, The security of practical quantum key distribution, Rev. Mod. Phys. **81**, 1301 (2009).

[52] F. Xu, X. Ma, Q. Zhang, H.-K. Lo, and J.-W. Pan, Secure quantum key distribution with realistic devices, Rev. Mod. Phys. **92**, 025002 (2020).

[53] P. Kómár, E. M. Kessler, M. Bishof, L. Jiang, A. S. Sørensen, J. Ye, and M. D. Lukin, A quantum network of clocks, Nat. Phys. **10**, 582 (2014).

[54] H. Dai, Q. Shen, C.-Z. Wang, S.-L. Li, W.-Y. Liu, W.-Q. Cai, S.-K. Liao, J.-G. Ren, J. Yin, Y.-A. Chen, Q. Zhang, F. Xu, C.-Z. Peng, and J.-W. Pan, Towards satellite-based quantum-secure time transfer, Nat. Phys. **11**, 25 (2020).

[55] J. Lee, L. Shen, A. Cerè, J. Troupe, A. Lamas-Linares, and C. Kurtsiefer, Asymmetric delay attack on an entanglement-based bidirectional clock synchronization protocol, Appl. Phys. Lett. **115**, 141101 (2019).

[56] C. Brunel, B. Lounis, P. Tamarat, and M. Orrit, Triggered Source of Single Photons Based on Controlled Single Molecule Fluorescence, Phys. Rev. Lett. **83**, 2722 (1999).

[57] R. Alléaume, F. Treussart, J.-M. Courty, and J.-F. Roch, Photon statistics characterization of a single-photon source, New J. Phys. **6**, 85 (2004).

[58] L. J. Martínez, T. Pelini, V. Waselowski, J. R. Maze, B. Gil, G. Cassabois, and V. Jacques, Efficient single photon emission from a high-purity hexagonal boron nitride crystal, Phys. Rev. B **94**, 121405 (2016).

[59] S. Isaac, A. Conrad, A. Hill, K. Herndon, B. Wilens, D. Chaffee, D. Sanchez-Rosales, R. Cochran, D. Gauthier, and P. Kwiat, in *Conference on Lasers and Electro-Optics* (Optical Society of America, San Jose, CA, USA, 2020), p. JW2A.16.

[60] A. Conrad, S. Isaac, R. Cochran, D. Sanchez-Rosales, B. Wilens, A. Gutha, T. Rezaei, D. Gauthier, and P. Kwiat, in *Free-Space Laser Communications XXXIII*, edited by H. Hemmati and D. M. Boroson (SPIE LASE, 2021), p. 29.

[61] D. E. Bruschi, T. C. Ralph, I. Fuentes, T. Jennewein, and M. Razavi, Spacetime effects on satellite-based quantum communications, Phys. Rev. D **90**, 045041 (2014).

[62] D. E. Bruschi, S. Chatzinotas, F. K. Wilhelm, and A. W. Schell, Spacetime effects on wavepackets of coherent light, Phys. Rev. D **104**, 085015 (2021).

[63] D. E. Bruschi, A. Datta, R. Ursin, T. C. Ralph, and I. Fuentes, Quantum estimation of the Schwarzschild spacetime parameters of the Earth, Phys. Rev. D **90**, 124001 (2014).

[64] J. Kohlrus, D. E. Bruschi, and I. Fuentes, Quantum-metrology estimation of spacetime parameters of the Earth outperforming classical precision, Phys. Rev. A **99**, 032350 (2019).

[65] I. Ali, N. Al-Dhahir, and J. E. Hershey, Doppler characterization for LEO satellites, IEEE Trans. Commun. **46**, 309 (1998).

[66] J. Yin, *et al.*, Satellite-based entanglement distribution over 1200 km, Science **356**, 1140 (2017).

[67] H. Bergeron, L. C. Sinclair, W. C. Swann, I. Khader, K. C. Cossel, M. Cermak, J.-D. Deschênes, and N. R. Newbury, Femtosecond time synchronization of optical clocks off of a flying quadcopter, Nat. Commun. **10**, 1819 (2019).

[68] H. Jin, F. M. Liu, P. Xu, J. L. Xia, M. L. Zhong, Y. Yuan, J. W. Zhou, Y. X. Gong, W. Wang, and S. N. Zhu, On-Chip Generation and Manipulation of Entangled Photons Based on Reconfigurable Lithium-Niobate Waveguide Circuits, Phys. Rev. Lett. **113**, 103601 (2014).

[69] X. Chen, Z. Fu, Q. Gong, and J. Wang, Quantum entanglement on photonic chips: A review, Adv. Photonics **3**, 064002 (2021).

[70] E. Brambila, R. Gómez, R. Fazili, M. Gräfe, and F. Steinlechner, Ultrabright polarization-entangled photon pair source for frequency-multiplexed quantum communication in free-space, ArXiv:2205.10214 (2022).

[71] M. Cabrejo-Ponce, C. Spiess, A. L. M. Muniz, P. Ancsin, and F. Steinlechner, Ghz-pulsed source of entangled photons for reconfigurable quantum networks, Quantum Sci. Technol. **7**, 045022 (2022).

[72] J. Savory, J. Sherman, and S. Romisch, in *2018 IEEE International Frequency Control Symposium (IFCS)* (IEEE, OlympicValley, CA, USA, 21.05.2018–24.05.2018), p. 1.

[73] G. Steinmeyer, D. H. Sutter, L. Gallmann, N. Matuschek, and U. Keller, Frontiers in ultrashort pulse generation: Pushing the limits in linear and nonlinear optics, Science **286**, 1507 (1999).

[74] A. L. Gaeta, M. Lipson, and T. J. Kippenberg, Photonic-chip-based frequency combs, Nat. Photonics **13**, 158 (2019).

[75] K. Predehl, G. Grosche, S. M. F. Raupach, S. Droste, O. Terra, J. Alnis, T. Legero, T. W. Hänsch, T. Udem, R. Holzwarth, and H. Schnatz, A 920-kilometer optical fiber link for frequency metrology at the 19th decimal place, Science (New York) **336**, 441 (2012).

[76] A. Lyons, G. C. Knee, E. Bolduc, T. Roger, J. Leach, E. M. Gauger, and D. Faccio, Attosecond-resolution Hong-Ou-Mandel interferometry, Sci. Adv. **4**, eaap9416 (2018).

[77] S.-Y. Baek, Y.-W. Cho, and Y.-H. Kim, Nonlocal dispersion cancellation using entangled photons, Opt. Express **17**, 19241 (2009).

[78] J. Troupe and A. Lamas-Linares, in *Advances in Photonics of Quantum Computing, Memory, and Communication XI*, edited by Z. U. Hasan, P. R. Hemmer, A. L. Migdall, and A. E. Craig (SPIE OPTO, San Francisco, California, United States, 2018), p. 20.

[79] J. Zhao, C. Ma, M. Rüsing, and S. Mookherjea, High Quality Entangled Photon Pair Generation in Periodically Poled Thin-Film Lithium Niobate Waveguides, Phys. Rev. Lett. **124**, 163603 (2020).

[80] J. He, B. A. Bell, A. Casas-Bedoya, Y. Zhang, A. S. Clark, C. Xiong, and B. J. Eggleton, Ultracompact quantum splitter of degenerate photon pairs, Optica **2**, 779 (2015).

[81] C. Xiong, C. Monat, A. S. Clark, C. Grillet, G. D. Marshall, M. J. Steel, J. Li, L. O'Faolain, T. F. Krauss, J. G. Rarity, and B. J. Eggleton, Slow-light enhanced correlated photon pair generation in a silicon photonic crystal waveguide, Opt. Lett. **36**, 3413 (2011).

[82] J. Vanier and L.-G. Bernier, On the signal-to-noise ratio and short-term stability of passive rubidium frequency standards, IEEE Trans. Instrum. Meas. **IM-30**, 277 (1981).

[83] B. M. Penrod, in *Proceedings of 1996 IEEE International Frequency Control Symposium* (Honolulu, HI, USA, 1996), p. 980.